

Optical conductivity of multi-Weyl semimetals

Seongjin Ahn¹, E. J. Mele^{2,*} and Hongki Min^{1,2†}

¹ *Department of Physics and Astronomy, Seoul National University, Seoul 08826, Korea and*

² *Department of Physics and Astronomy, University of Pennsylvania, Philadelphia, Pennsylvania 19104, USA*

(Dated: April 28, 2017)

Multi-Weyl semimetals are new types of Weyl semimetals which have anisotropic non-linear energy dispersion and a topological charge larger than one, thus exhibiting a unique quantum response. Using a unified lattice model, we calculate the optical conductivity numerically in the multi-Weyl semimetal phase and in its neighboring gapped states, and obtain the characteristic frequency dependence of each phase analytically using a low-energy continuum model. The frequency dependence of longitudinal and transverse optical conductivities obeys scaling relations that are derived from the winding number of the parent multi-Weyl semimetal phase and can be used to distinguish these electronic states of matter.

Introduction. A Weyl semimetal (WSM) is a gapless topological state of matter possessing \mathbf{k} -space singularities where its valence and conduction bands make contact at a point. This singularity is a \mathbf{k} -space monopole providing a quantized source or sink of a Berry's flux and can occur only in materials in which either time reversal symmetry or inversion symmetry is broken. In the prototypical WSM, a twofold band degeneracy at the Weyl point is broken linearly in momentum in all directions and the node is characterized by the topological winding number (also referred to as chirality) ± 1 . A transition to an insulating phase is possible only if Weyl nodes with opposite chirality pairwise merge and annihilate. The gapped phase produced by this merger can be in a normal insulating state or a topological quantum anomalous Hall state. The linear dispersion around the Weyl point has important consequences for the low frequency optical properties, which have been explored theoretically and used as an experimental fingerprint of the topological state [1–9].

A \mathbf{k} -space merger of Weyl points with the *same* chirality produces a new type of Weyl semimetal, referred to as a multi-Weyl semimetal (m-WSM) [10, 11]. In these states, the merger of the nodes is robust if it is protected by a point group symmetry. The low energy dispersion can then be characterized by double (triple) Weyl nodes with linear dispersion along one symmetry direction and quadratic (cubic) dispersion along the remaining two directions. Because of the change in topological nature, the enhancement of the density of states, the anisotropic non-linear energy dispersion and a modified spin-momentum locking structure, these states will have optical and transport signatures that distinguish them from elementary WSMs.

In this Rapid Communication, we report calculations of the optical conductivity in m-WSMs, and analyze their characteristic frequency dependence in the semimetallic state and in nearby insulating states, focusing on the ef-

fects of the winding number, lattice regularization and phase transitions. We find that the results for m-WSMs can be clearly distinguished from those for WSMs by their low-energy frequency dependence, which is determined by the winding number of the m-WSM phase.

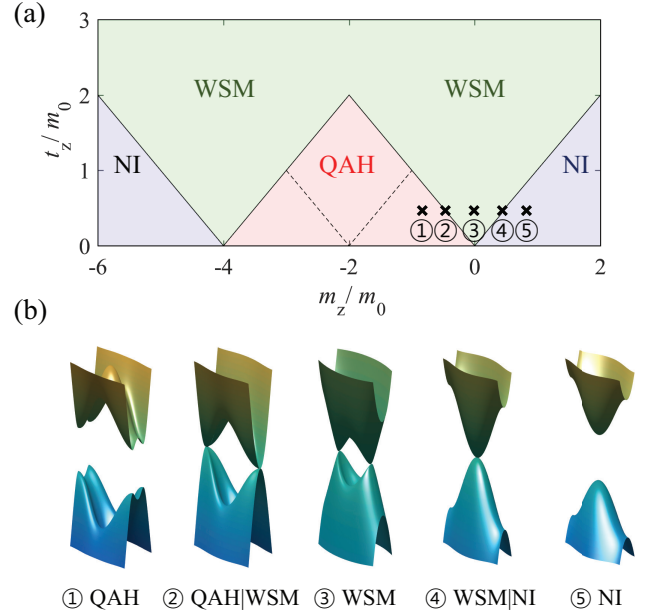


FIG. 1: (a) Phase diagrams of $J = 2$ lattice models on the t_z/m_0 and m_z/m_0 plane and (b) evolution of the energy band structure from the 3D quantum anomalous Hall (QAH) phase to the normal insulator (NI) phase. Here, we use several values of m_z/m_0 corresponding to different phases, indicated by circled numbers in the phase diagram. QAH|WSM and WSM|NI denote the transition phase between 3D QAH and WSM, and WSM and NI, respectively. The phase diagram for $J = 1$ has a similar shape, but has a different phase boundary between the WSM and 3D QAH represented by the dashed line [12].

Model. The low-energy effective Hamiltonian for m-WSMs of order J near a single Weyl point can be described by the Hamiltonian:

$$H_J = \varepsilon_0 \left(\tilde{k}_-^J \sigma_+ + \tilde{k}_+^J \sigma_- \right) + \hbar v_z k_z \sigma_z, \quad (1)$$

*Electronic address: mele@physics.upenn.edu

†Electronic address: hmin@snu.ac.kr

where $\tilde{k}_\pm = k_\pm/k_0$ with $k_\pm = k_x \pm ik_y$, $\sigma_\pm = \frac{1}{2}(\sigma_x \pm i\sigma_y)$, and σ are Pauli matrices acting in the space of two bands that make contact at the Weyl point. Here, v_z is the effective velocity along the k_z direction, and k_0 and ε_0 are material dependent parameters in units of momentum and energy, respectively. For simplicity, we assumed the axial symmetry around the k_z -axis. Note that the eigenenergies of the Hamiltonian are given by $\varepsilon_\pm = \pm\sqrt{\varepsilon_0^2\tilde{k}_\parallel^{2J} + (\hbar v_z k_z)^2}$ where $\tilde{k}_\parallel = \sqrt{\tilde{k}_x^2 + \tilde{k}_y^2}$, and the in-plane energy dispersion is characterized by J . Thus the winding number determines not only the topological nature of the wave function but also the anisotropic energy dispersion of the system.

Let us consider a lattice model that shows at some parameter range the m-WSM phase described by Eq. (1). A simple lattice model for the Weyl semimetals with $J = 1$ which has inversion symmetry with broken time-reversal symmetry is given by [12–14]

$$\begin{aligned} H_1 &= t_x \sin(k_x a) \sigma_x + t_y \sin(k_y a) \sigma_y + M_z \sigma_z, \\ M_z &= m_z - t_z \cos(k_z a) + m_0 [2 - \cos(k_x a) - \cos(k_y a)], \end{aligned} \quad (2)$$

where a is the lattice spacing, and $t_{x,y,z}$, m_z and m_0 are material dependent parameters. Similarly, we can generalize the above lattice model in Eq. (2) to $J = 2$ so that near the Weyl points the low-energy Hamiltonian reduces to the form of Eq. (1) [15]:

$$\begin{aligned} H_2 &= t_x [\cos(k_y a) - \cos(k_x a)] \sigma_x \\ &+ t_y \sin(k_x a) \sin(k_y a) \sigma_y + M_z \sigma_z. \end{aligned} \quad (3)$$

Depending on the model parameters, the Hamiltonian in Eqs. (2) and (3) shows various phases such as normal insulators (NIs), Weyl semimetals, and three-dimensional (3D) quantum anomalous Hall (QAH) states, as shown in Fig. 1 along with the corresponding energy band structures. The phase diagram for $J = 2$ has a similar shape to that for $J = 1$ [12], but because of the change in the electronic structure, the optical properties in the m-WSMs show a strong dependence on their chirality.

For the continuum model corresponding to each phase, we choose the parameter range where Weyl nodes arise at $(k_x, k_y) = (0, 0)$. Other choices of parameter ranges give fundamentally identical settings. Using the $\mathbf{k} \cdot \mathbf{p}$ method, we can write a generic continuum model for various phases as [16]

$$H = \varepsilon_0 \left(\tilde{k}_-^J \sigma_+ + \tilde{k}_+^J \sigma_- \right) + M_z \sigma_z, \quad (4)$$

where the mass term is given by $M_z \approx \hbar v_z q_z + \alpha + \beta q_z^2 + \gamma(k_x^2 + k_y^2)$. Here we set $\gamma = \frac{m_0 a^2}{2} > 0$ except for the WSM phase with $\gamma = 0$ where the linear term in M_z dominates over the quadratic term associated with γ at low energies. Note that for the NI (3D QAH) phase, $\alpha = m_z \mp t_z$ and $\beta = \pm \frac{t_z a^2}{2}$. Then, for each phase, we

find

$$\begin{aligned} \text{NI} &: q_z = k_z; \quad v_z = 0; \quad \alpha, \beta > 0, \\ \text{NI|WSM} &: q_z = k_z; \quad v_z = 0; \quad \alpha = 0, \beta > 0, \\ \text{WSM} &: q_z = k_z \mp b; \quad v_z \neq 0; \quad \alpha = \beta = 0, \\ \text{WSM|QAH} &: q_z = k_z \mp \frac{\pi}{a}; \quad v_z = 0; \quad \alpha = 0, \beta < 0, \\ \text{QAH} &: q_z = k_z \mp \frac{\pi}{a}; \quad v_z = 0; \quad \alpha, \beta < 0, \end{aligned} \quad (5)$$

where $\cos(ba) \equiv m_z/t_z$ with $|m_z|/t_z < 1$. For calculation, we set $k_0 = 1/a$, $t_x = t_y = 4m_0$ and $t_z = 0.5m_0$ with $m_0 > 0$, and vary $-m_0 < m_z < m_0$ with other parameters fixed to induce various phases.

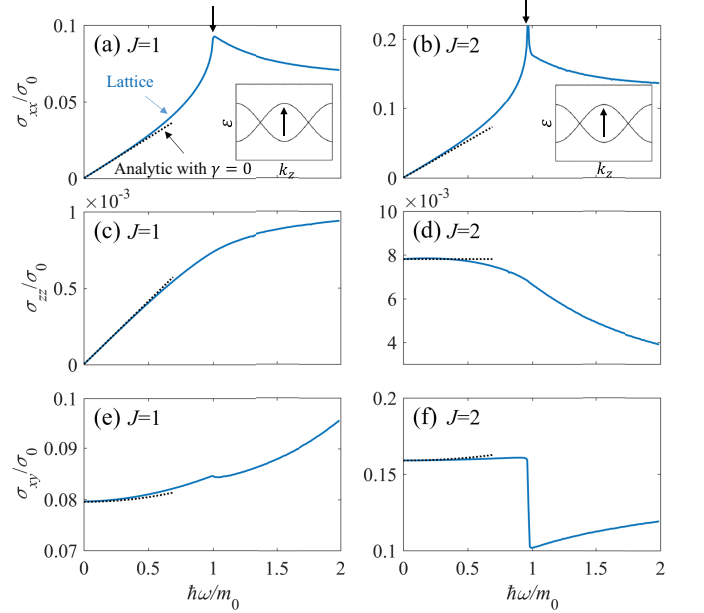


FIG. 2: Real part of (a)-(d) longitudinal and (e), (f) transverse optical conductivities in units of $\sigma_0 = \frac{e^2}{\hbar a}$ for the lattice (blue solid line) and continuum (black dotted line) models in the WSM phase. The arrows in the insets indicate interband transitions corresponding to kink structures in $\sigma_{xx}(\omega)$ and $\sigma_{xy}(\omega)$. Here, $m_z/m_0 = 0$, $b = 0.5\pi/a$, and $k_c = \pi/a$ are used for calculation.

Optical conductivity. The Kubo formula for the optical conductivity in the non-interacting limit can be expressed as [17]

$$\begin{aligned} \sigma_{ij}(\omega) &= -\frac{ie^2}{\hbar} \sum_{s,s'} \int \frac{d^3k}{(2\pi)^3} \frac{f_{s,\mathbf{k}} - f_{s',\mathbf{k}}}{\varepsilon_{s,\mathbf{k}} - \varepsilon_{s',\mathbf{k}}} \\ &\times \frac{M_i^{ss'}(\mathbf{k}) M_j^{s's}(\mathbf{k})}{\hbar\omega + \varepsilon_{s,\mathbf{k}} - \varepsilon_{s',\mathbf{k}} + i0^+}, \end{aligned} \quad (6)$$

where $i, j = x, y, z$, $f_{s,\mathbf{k}} = 1/[1 + e^{(\varepsilon_{s,\mathbf{k}} - \mu)/k_B T}]$ is the Fermi distribution function, μ is the chemical potential, and $M_i^{ss'}(\mathbf{k}) = \langle s, \mathbf{k} | \hbar \hat{v}_i | s', \mathbf{k} \rangle$, with the velocity operator \hat{v}_i obtained from the relation $\hat{v}_i = \frac{1}{\hbar} \frac{\partial \hat{H}}{\partial k_i}$.

In the following, we consider only the undoped case with $\mu = 0$. In the clean limit at zero temperature, the

real part of the longitudinal optical conductivity for m-WSMs within the continuum model is given by [16]

$$\sigma_{xx}(\omega) = \frac{g_N}{24\pi} \frac{J e^2}{\hbar v_z} \omega, \quad (7a)$$

$$\sigma_{zz}(\omega) = \frac{g_N}{24\pi} \frac{e^2 v_z}{\hbar v_{\parallel}^2} A_{zz}^{\text{WSM}} \left(\frac{\omega}{\omega_0} \right)^{\frac{2}{J}-1} \omega_0, \quad (7b)$$

where $g_N = 2$ is the number of nodes, $\varepsilon_0 = \hbar\omega_0 = \hbar v_{\parallel} k_0$, $A_{zz}^{\text{WSM}} = \frac{3\sqrt{\pi}\Gamma(\frac{1}{J})}{2^{\frac{2}{J}} J^2 \Gamma(\frac{1}{J} + \frac{3}{2})}$, and $\Gamma(x)$ is the gamma function [18]. Note that $\sigma_{xx}(\omega) \propto J\omega$ while $\sigma_{zz} \propto \omega^{\frac{2}{J}-1}$, exhibiting the chirality dependent power-law exponents in frequencies. Also note that the effect of a finite μ simply produces a small gap due to Pauli blocking in interband transitions and a conventional Drude peak from intra-band transitions, which does not alter the characteristic frequency dependence of the conductivity as long as μ is not high enough that the effective Hamiltonian is still characterized by a m-WSM Hamiltonian [16].

Next, consider the real part of the Hall or transverse optical conductivity. Note that a sign change of M_z in the Brillouin zone can produce a nontrivial state that supports a Hall effect in the k_x - k_y plane for a fixed k_z . We therefore focus only on the in-plane off-diagonal part $\sigma_{xy}(\omega)$. If two Weyl nodes with opposite chirality are located at $\pm\mathbf{b} = \pm b\hat{z}$, the real part of the Hall conductivity up to second order in ω is given by

$$\sigma_{xy}(\omega) = J\chi \frac{e^2}{\hbar} \left(\frac{b}{2\pi^2} + \frac{1}{24\pi^2 v_z^2} \frac{b}{k_c^2 - b^2} \omega^2 \right), \quad (8)$$

where k_c is the cutoff along the k_z direction. Here, χ represents the right-handed/left-handed chirality, which has $\chi = \pm 1$ if the node with positive chirality is at $\pm b\hat{z}$ and the other at $\mp b\hat{z}$. Note that the Hall conductivity for m-WSMs is given by J times that for $J = 1$ Weyl semimetals, thus their surface states could be manifested by J Fermi arcs connecting the two Weyl nodes.

Figure 2 shows the calculated optical conductivities for $J = 1$ and $J = 2$ lattice and continuum models, respectively. At low frequencies, the lattice models are approximated by the corresponding low energy model in Eq. (1), thus the optical conductivities obtained from the lattice and continuum models are in good agreement. As the frequency increases, however, optical conductivities deviate from the continuum model and show a kink structure in $\sigma_{xx}(\omega)$ and $\sigma_{xy}(\omega)$ at $\hbar\omega = 2|m_z - t_z|$ due to the interband transitions between states around the van Hove singularity [8], as shown in the insets to (a) and (b).

For the NI phase ($\alpha > 0$) and 3D QAH phase ($\alpha < 0$), we obtain the leading-order ω dependence of longitudinal optical conductivities analytically assuming $\gamma = 0$ in the vicinity of $\hbar\omega = 2|\alpha|$,

$$\sigma_{xx}(\omega) \sim (\hbar\omega - 2|\alpha|)^{\frac{1}{2}} \Theta(\hbar\omega - 2|\alpha|), \quad (9a)$$

$$\sigma_{zz}(\omega) \sim (\hbar\omega - 2|\alpha|)^{\frac{1}{J} + \frac{3}{2}} \Theta(\hbar\omega - 2|\alpha|). \quad (9b)$$

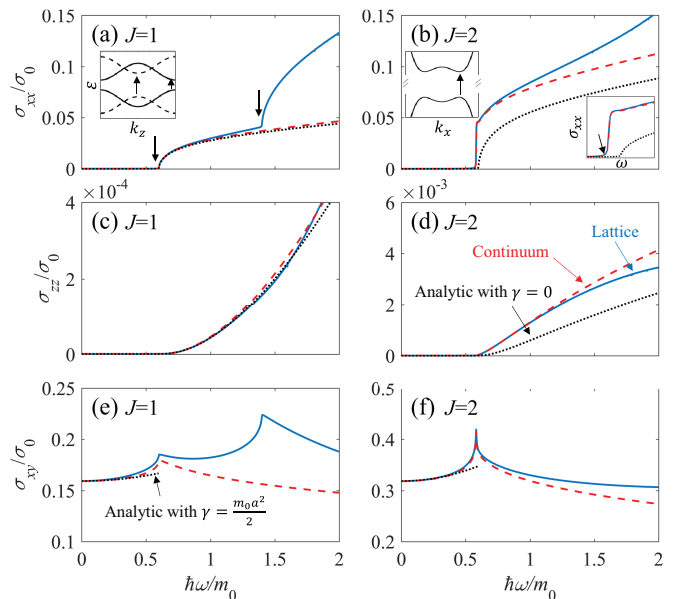


FIG. 3: Real part of (a)-(d) longitudinal and (e), (f) transverse optical conductivities in the 3D QAH phase for the lattice model (blue solid line), the continuum model (red dashed line), and the analytic results (black dotted line). For the longitudinal (transverse) conductivities, the analytic results are obtained for $\gamma = 0$ ($\gamma = \frac{m_0 a^2}{2}$). Solid (dashed) lines in the inset to (a) represent the energy dispersion for $J = 1$ along the k_z direction with $k_x = 0$ ($k_x = \frac{\pi}{a}$) and $k_y = 0$. The left inset to (b) represents the energy dispersion for $J = 2$ along the k_x direction with $k_z = \frac{\pi}{a}$ and $k_y = 0$, and the right inset to (b) shows an enlarged view in $\sigma_{xx}(\omega)$ near the interband transition. Arrows in the insets indicate interband transitions corresponding to the kink structures appearing in σ_{xx} and σ_{xy} . Here, $m_z/m_0 = -0.8$ and $k_c = \pi/a$ are used for the calculation.

Note that similarly to the WSM phase, $\sigma_{xx}(\omega)$ has the same ω dependence regardless of the chirality index J , while $\sigma_{zz}(\omega)$ has different power-law exponents depending on J . Here the analytic results are obtained assuming $\gamma = 0$ for simplicity, which is valid when the effect of the band distortion associated with nonzero γ is small ($\gamma k_0^2 \ll \varepsilon_0$ or $m_0 \ll t_x, t_y$). As $\gamma k_0^2/\varepsilon_0$ increases, the power-law exponent deviates from the analytic expression in Eq. (9) obtained assuming $\gamma = 0$, and the derivation is more significant for $J = 2$ than $J = 1$ because the kinetic term associated with J is comparable to the quadratic γ term at low frequencies [16].

The transverse optical conductivities in the NI and 3D QAH phases up to second order in ω are given by

$$\sigma_{xy}(\omega) = \xi \sigma_{xy}^{\text{QAH}} + \frac{e^2}{\hbar} B_{xy} \omega^2, \quad (10)$$

where $\sigma_{xy}^{\text{QAH}} = \frac{J e^2}{\hbar} \frac{k_c}{2\pi^2}$ and $\xi = 0$ ($\xi = 1$) for the NI (3D QAH) phase. The static part ($\omega = 0$) in Eq. (10) can be obtained after properly subtracting the residual term, because the static Hall conductivity for the continuum model is not properly regularized carrying an arbitrary

residual value. Thus only the difference in this quantity between different electronic states is experimentally measurable, giving a quantized value in the 3D QAH phase while zero in the NI phase. In this sense, we choose the momentum cutoff along the k_z direction as $k_c = \pi/a$ so that the properly subtracted static Hall conductivity in the 3D QAH phase has the same quantized value as in the lattice model. A detailed discussion on the regularization process and the expression for B_{xy} can be found in the Supplemental Material [16]. Note that for the transverse optical conductivities, we present analytic results with non-zero γ .

Figure 3 shows calculated optical conductivities for the $J = 1$ and $J = 2$ lattice and continuum models in the 3D QAH phase. If $\gamma = 0$, the energy gap with a size of $2|\alpha|$ for both NI and 3D QAH phases leads to zero conductivity for frequencies $\hbar\omega < 2|\alpha|$ due to the optical gap. Because of the non-zero γ , a Mexican hat structure appears in the 3D QAH phase (but not in the NI phase) if $\alpha < \alpha_c = -\frac{e_0^2}{2\gamma k_0^2}$ for $J = 1$, and if $\alpha < 0$ for $J = 2$ exhibiting a shifted interband peak with respect to the $\gamma = 0$ result [16]. For the $J = 1$ lattice model in the 3D QAH phase, an additional kink structure appears at $\hbar\omega = 2|m_z - t_z + 2m_0|$ due to the interband transitions at local minima $(k_x, k_y, k_z) = (\pm\frac{\pi}{a}, 0, 0), (0, \pm\frac{\pi}{a}, 0)$, as shown in Fig. 3(a).

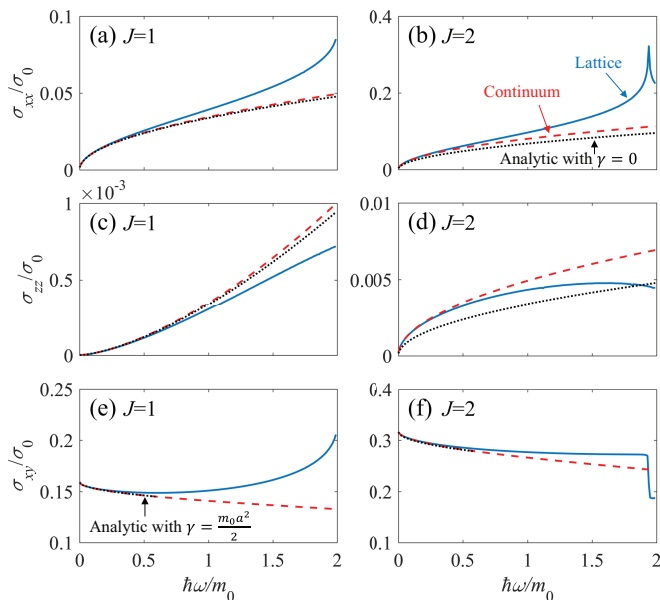


FIG. 4: Real part of (a)-(d) longitudinal and (e), (f) transverse optical conductivities at the transition between the 3D QAH and WSM phases for the lattice model (blue solid line), the continuum model (red dashed line), and the analytic results (black dotted line). For the longitudinal (transverse) conductivities, the analytic results are obtained for $\gamma = 0$ ($\gamma = \frac{m_0 a^2}{2}$). Here, $m_z/m_0 = -0.5$ and $k_c = \pi/a$ are used for calculation.

At the transition point between the WSM and NI phases or between the WSM and 3D QAH phases, the

longitudinal (transverse) optical conductivities obtained assuming a zero (non-zero) γ are given by

$$\sigma_{xx}(\omega) = \frac{e^2}{\hbar} A_{xx}(\hbar\omega)^{\frac{1}{2}}, \quad (11a)$$

$$\sigma_{zz}(\omega) = \frac{e^2}{\hbar} A_{zz}(\hbar\omega)^{\frac{2}{J}-\frac{1}{2}}, \quad (11b)$$

$$\sigma_{xy}(\omega) = \xi \sigma_{xy}^{\text{QAH}} + \frac{e^2}{\hbar} C_{xy} \omega^\nu. \quad (11c)$$

Note that similarly as in the NI and 3D QAH phases, the static part of $\sigma_{xy}(\omega)$ should be properly subtracted by the residual term. The expressions for A_{xx} and A_{zz} can be found in the Supplemental Material [16]. Here, the exponent $\nu \approx 0.5$ is found numerically for $J = 1, 2$ with a frequency independent coefficient C_{xy} . Note that the longitudinal conductivities for both transition points are identical (within a $\gamma = 0$ approximation), whereas the Hall conductivities have different static values, with the difference given by σ_{xy}^{QAH} .

Discussion — Recently, Huang *et al.* [19] demonstrated that strontium silicide (SrSi₂) hosts double Weyl nodes with a chirality $J = 2$. The effective Hamiltonian, which describes one of the Weyl nodes with a chirality $J = 2$ in SrSi₂, resembles that of bilayer graphene with the interlayer hopping replaced by the spin-orbit coupling Δ connecting the two $J = 1$ Weyl Hamiltonians. If we assume $\mu = 0$, at low frequencies the optical conductivity for the double Weyl nodes in SrSi₂ behaves similar to that of the $J = 2$ Weyl semimetals, showing $\sigma_{xx} \sim \omega$ and $\sigma_{zz} \sim \omega^0$ dependence, whereas at high frequencies, the optical conductivity shows two copies of the $J = 1$ Weyl semimetals exhibiting a linear ω dependence in σ_{xx} and σ_{zz} . At intermediate frequencies, kink structures appear at frequencies comparable to the energy scales of interband transitions determined by Δ . Note that the double Weyl nodes in SrSi₂ are not actually located at $\mu = 0$, thus the longitudinal conductivity in real SrSi₂ will give additional features of the Pauli blocking and the Drude peak. In addition, in a real sample, multiple Weyl nodes coexist, thus the optical conductivity can be obtained by the sum of the contribution from each node. Tilt and impurities will also affect the optical conductivity. However, the characteristic frequency dependence described here will not be altered above the frequency corresponding to the energy scale of the tilt or impurity potential [16].

In summary, we studied the optical properties of m-WSMs in semimetallic and nearby insulating phases, focusing on the frequency dependence of optical conductivity. We demonstrated that the optical conductivities $\sigma_{xx}(\omega)$, $\sigma_{zz}(\omega)$ and $\sigma_{xy}(\omega)$ show a characteristic frequency dependence that strongly varies according to the winding number and phase of the system, and thus can be used as a spectroscopic signature of m-WSMs.

Acknowledgments

This research was supported by the Basic Science Research Program through the National Research Foundation of Korea (NRF) funded by the Ministry of Education under Grant No. 2015R1D1A1A01058071. EJM's work

on this project was supported by the U.S. Department of Energy, Office of Basic Energy Sciences under Award No. DE-FG02-ER45118. HM acknowledges travel support provided by the University Research Foundation at the University of Pennsylvania while this work was carried out.

-
- [1] Xiangang Wan, Ari M. Turner, Ashvin Vishwanath, and Sergey Y. Savrasov, Topological semimetal and Fermi-arc surface states in the electronic structure of pyrochlore iridates, *Phys. Rev. B* **83**, 205101 (2011).
- [2] Pavan Hosur, S. A. Parameswaran, and Ashvin Vishwanath, Charge Transport in Weyl Semimetals, *Phys. Rev. Lett.* **108**, 046602 (2012).
- [3] Phillip E. C. Ashby and J. P. Carbotte, Chiral anomaly and optical absorption in Weyl semimetals, *Phys. Rev. B* **89**, 245121 (2014).
- [4] A. B. Sushkov, J. B. Hofmann, G. S. Jenkins, J. Ishikawa, S. Nakatsuji, S. Das Sarma, and H. D. Drew, Optical evidence for a Weyl semimetal state in pyrochlore $\text{Eu}_2\text{Ir}_2\text{O}_7$, *Phys. Rev. B* **92**, 241108(R) (2015).
- [5] R. Y. Chen, S. J. Zhang, J. A. Schneeloch, C. Zhang, Q. Li, G. D. Gu, and N. L. Wang, Optical spectroscopy study of the three-dimensional Dirac semimetal ZrTe_5 , *Phys. Rev. B* **92**, 075107 (2015).
- [6] B. Xu, Y. M. Dai, L. X. Zhao, K. Wang, R. Yang, W. Zhang, J. Y. Liu, H. Xiao, G. F. Chen, A. J. Taylor, D. A. Yarotski, R. P. Prasankumar, and X. G. Qiu, Optical spectroscopy of the Weyl semimetal TaAs, *Phys. Rev. B* **93**, 121110(R) (2016).
- [7] C. J. Tabert, J. P. Carbotte, and E. J. Nicol, Optical and transport properties in three-dimensional Dirac and Weyl semimetals, *Phys. Rev. B* **93**, 085426 (2016).
- [8] C. J. Tabert and J. P. Carbotte, Optical conductivity of Weyl semimetals and signatures of the gapped semimetal phase transition, *Phys. Rev. B* **93**, 085442 (2016).
- [9] D. Neubauer, J. P. Carbotte, A. A. Nateprov, A. Lhle, M. Dressel, and A. V. Pronin, Interband optical conductivity of the [001]-oriented Dirac semimetal Cd_3As_2 , *Phys. Rev. B* **93**, 121202(R) (2016).
- [10] G. Xu, H. Weng, Z. Wang, X. Dai, and Z. Fang, Chern Semimetal and the Quantized Anomalous Hall Effect in HgCr_2Se_4 , *Phys. Rev. Lett.* **107**, 186806 (2011).
- [11] C. Fang, M. J. Gilbert, X. Dai, and B. A. Bernevig, Multi-Weyl Topological Semimetals Stabilized by Point Group Symmetry, *Phys. Rev. Lett.* **108**, 266802 (2012).
- [12] Chui-Zhen Chen, Juntao Song, Hua Jiang, Qing-feng Sun, Ziqiang Wang, and X.C. Xie, Disorder and Metal-Insulator Transitions in Weyl Semimetals, *Phys. Rev. Lett.* **115**, 246603 (2015).
- [13] P. Delplace, J. Li and D. Carpentier, Topological Weyl semi-metal from a lattice model, *EPL* **97**, 67004 (2012).
- [14] Ari M. Turner and Ashvin Vishwanath, Beyond Band Insulators: Topology of Semi-metals and Interacting Phases, arXiv:1301.0330 (2013).
- [15] Shao-Kai Jian and Hong Yao, Correlated double-Weyl semimetals with Coulomb interactions: Possible applications to HgCr_2Se_4 and SrSi_2 , *Phys. Rev. B* **92**, 045121 (2015).
- [16] See Supplemental Material for details of the continuum model and corresponding energy dispersion at each phase, the analytic expressions for optical conductivities in various phases, and the effects of γ , impurities, chemical potential and tilt.
- [17] Gerald D. Mahan, *Many-particle physics*, 3rd ed., Springer (2000).
- [18] George B. Arfken, Hans J. Weber, and Frank E. Harris, *Mathematical Methods for Physicists*, 7th ed. (Academic, New York, 2012).
- [19] S.-M. Huang, S.-Y. Xu, I. Belopolski, C.-C. Lee, G. Chang, T.-R. Chang, B. Wang, N. Alidoust, G. Bian, M. Neupane, D. Sanchez, H. Zheng, H.-T. Jeng, A. Bansil, T. Neupert, H. Lin, and M. Z. Hasan, New type of Weyl semimetal with quadratic double Weyl fermions, *Proc. Natl. Acad. Sci. U.S.A* **113**, 1180 (2016).

Supplemental Material: Optical conductivity of multi-Weyl semimetals

Seongjin Ahn¹, E. J. Mele², and Hongki Min^{1,2}

¹ *Department of Physics and Astronomy, Seoul National University, Seoul 08826, Korea and*

² *Department of Physics and Astronomy, University of Pennsylvania, Philadelphia, PA 19104, USA*

I. CONTINUUM MODEL FOR EACH PHASE IN MULTI-WEYL SEMIMETALS

In this section, we discuss a continuum model for each phase in the phase diagram, including the transition point. For the calculation, we set $k_0 = 1/a$, $t_x = t_y = 4m_0$ and $t_z = 0.5m_0$ with $m_0 > 0$, and vary $-m_0 < m_z < m_0$ with other parameters fixed to induce various phases.

A. WSM phase

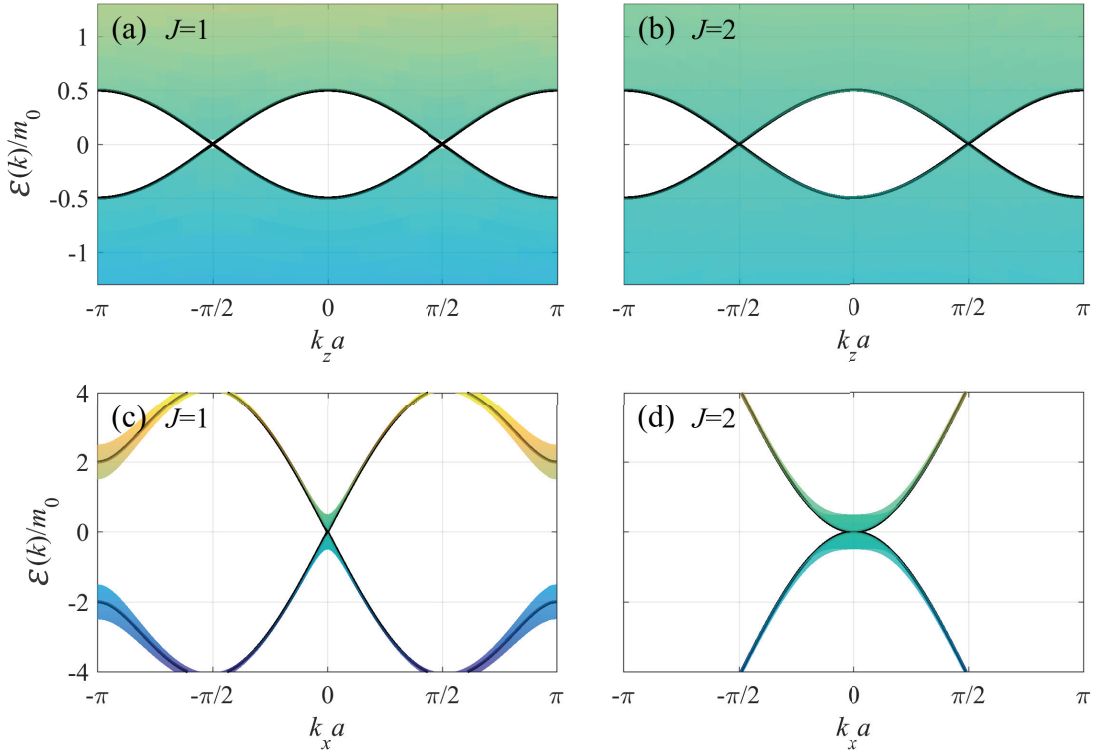


FIG. 1: Energy dispersions for the $J = 1$ and $J = 2$ lattice models in the WSM phase viewed from the k_z - and k_x -axes. Shaded regions represent the energy dispersions obtained by projecting them to (a), (b) the k_z -axis or to (c), (d) the k_x -axis at $k_y = 0$, in which each point of the dispersion is colored according to the energy scale, with yellow (blue) indicating higher (lower) values. The black solid lines are added to represent the energy dispersions across the Weyl node along (a), (b) the k_z -axis with $k_x = 0$ and (c), (d) the k_x -axis with $k_z = b$. Here, $m_z/m_0 = 0$ and $b = 0.5\pi/a$ are used for calculation.

First, consider a continuum model for the WSM phase. For $|m_z|/t_z < 1$ with $\cos(ba) \equiv m_z/t_z$, two Weyl points appear at $\mathbf{k} = \pm b\hat{z}$, at which the conduction and valence bands touch at zero energy. Then, the Hamiltonian for $J = 1$ reduces to the form for Weyl semimetals:

$$H_1 \approx \hbar v_x k_x \sigma_x + \hbar v_y k_y \sigma_y \pm \hbar v_z q_z \sigma_z, \quad (1)$$

where $q_z = k_z \mp b$, $\frac{\hbar v_x}{a} = t_x$, $\frac{\hbar v_y}{a} = t_y$ and $\frac{\hbar v_z}{a} = t_z \sin(ba)$. Similarly, for $J = 2$, the Hamiltonian H_2 reduces to Eq. (1) of the main text with $J = 2$, where $\varepsilon_0 = \frac{1}{2}t_{\parallel}(k_0 a)^2$ with $t_x = t_y \equiv t_{\parallel}$ and $\frac{\hbar v_z}{a} = t_z \sin(ba)$. Note that the

two Weyl points located at $\mathbf{k} = \pm b\hat{z}$ have opposite handedness $\chi = \pm 1$, representing the right-handed/left-handed chirality with Chern number χJ .

Figure 1 shows the energy dispersion for the $J = 1$ and $J = 2$ lattice models in the WSM phase. As shown in Eq. (1) of the main text, the energy dispersion near the Weyl point along the k_z direction with $k_x = k_y = 0$ is linear, while that along the k_x - k_y directions with $k_z = 0$ is proportional to k^J . Note that there always appear multiple Weyl points in the Brillouin zone with the total chirality summing to zero, and in the lattice model we are considering, there are two Weyl nodes with opposite chiralities. Between the two Weyl points, the energy dispersion becomes flat along the k_z direction at $k_x = k_y = 0$, showing a van Hove singularity, which gives rise to an interband transition peak in the optical conductivity, as shown in Fig. 2 in the main text.

B. NI phase

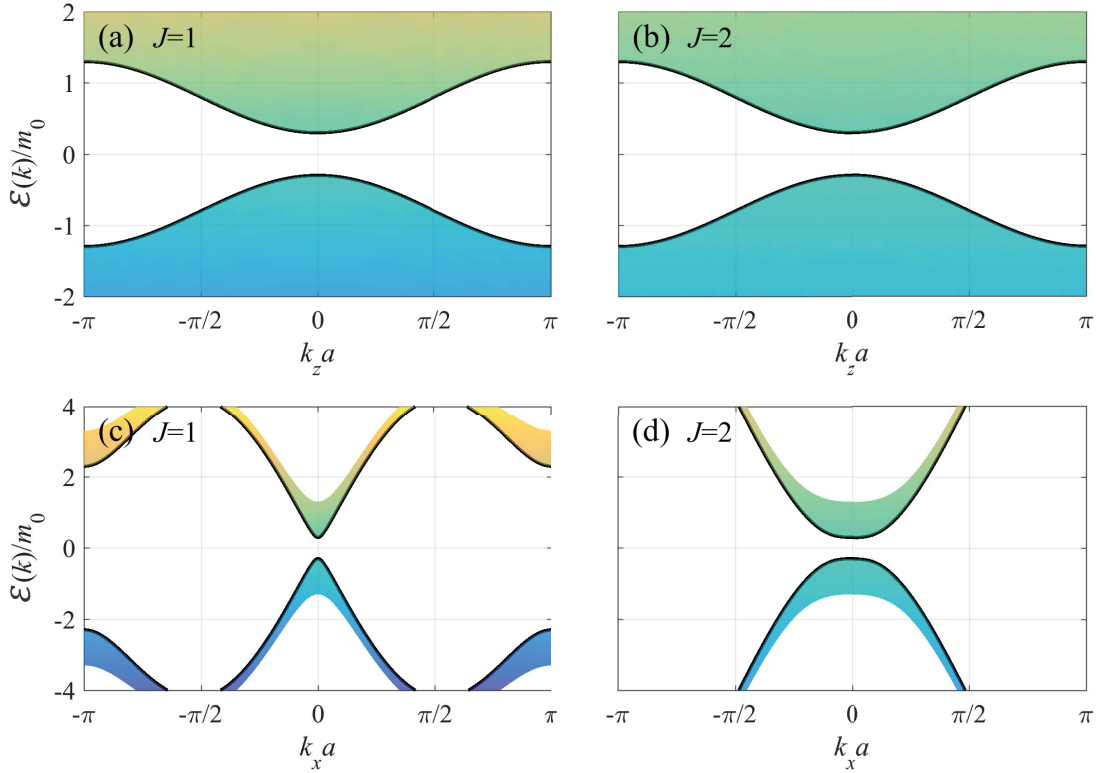


FIG. 2: Energy dispersions for the (a), (c) $J = 1$ and (b), (d) $J = 2$ lattice models in the NI phase viewed from the (a), (b) k_z - and (c), (d) k_x -axes with $k_y = 0$. Here, $m_z/m_0 = 0.8$ is used for the calculation.

For $m_z > t_z$, the mass term M_z defined in Eq. (2) of the main text remains positive throughout the Brillouin zone, thus the system is in the trivial insulator phase. Near $\mathbf{k} = (0, 0, 0)$, M_z can be approximated as

$$M_z \approx m_z - t_z + \frac{t_z a^2}{2} k_z^2 + \frac{m_0 a^2}{2} (k_x^2 + k_y^2). \quad (2)$$

Figure 2 shows the energy dispersions for the $J = 1$ and $J = 2$ lattice models with an energy gap of the size of 2α , where $\alpha = m_z - t_z$, which gives rise to a corresponding optical gap.

C. 3D QAH phase

For $m_z < -t_z$, the mass term M_z changes its sign in the Brillouin zone, generating a non-trivial insulating phase in contrast to the case of the NI phase. Near $\mathbf{k} = (0, 0, \pm \frac{\pi}{a})$, M_z can be approximated as

$$M_z \approx m_z + t_z - \frac{t_z a^2}{2} q_z^2 + \frac{m_0 a^2}{2} (k_x^2 + k_y^2), \quad (3)$$

where $q_z = k_z \mp \frac{\pi}{a}$.

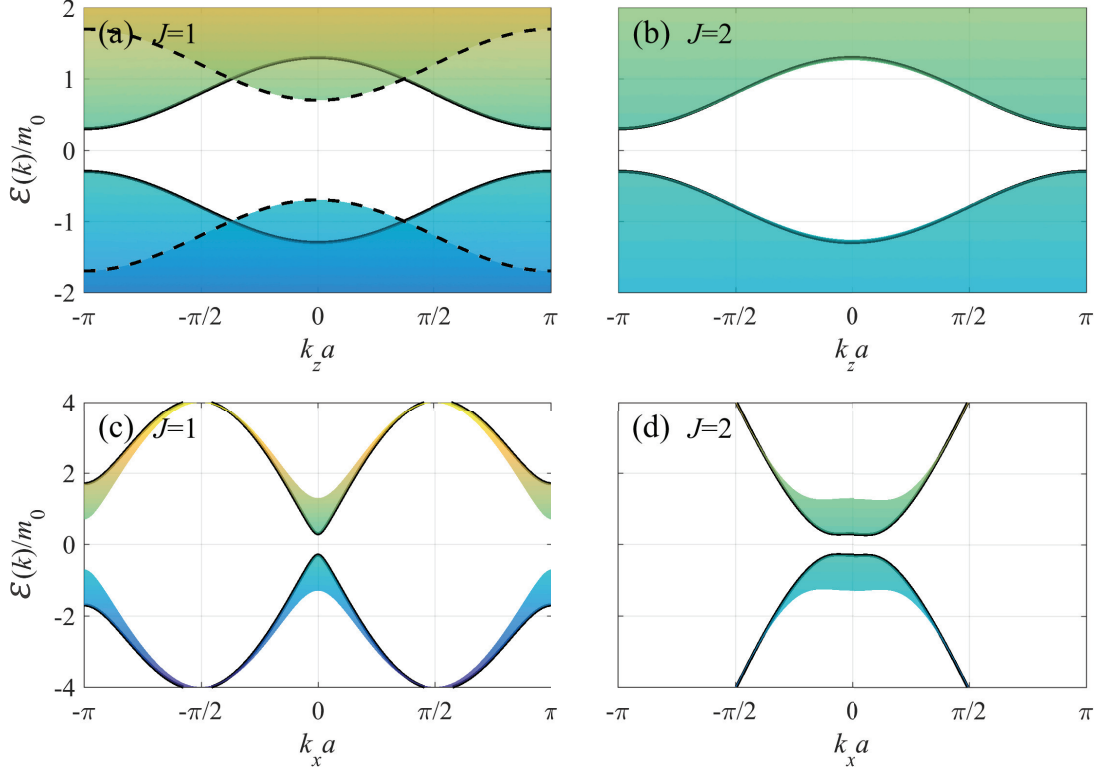


FIG. 3: Energy dispersions for the (a), (c) $J = 1$ and (b), (d) $J = 2$ lattice models in the 3D QAH phase viewed from the (a), (b) k_z - and (c), (d) k_x -axes with $k_y = 0$. Here, $m_z/m_0 = -0.8$ is used for the calculation. The dashed lines in (a) represent the energy dispersion along the k_z -axis with $k_x = \frac{\pi}{a}$ and $k_y = 0$. Note that the interband transition between the dashed bands at $k_z = 0$ corresponds to the second peak in $\sigma_{xx}(\omega)$, as shown in Fig. 3(a) in the main text.

Figure 3 shows the energy dispersion for the $J = 1$ and $J = 2$ lattice models in the 3D QAH phase. Because of the negative sign of the constant term $\alpha = m_z + t_z < 0$ in M_z , the 3D QAH phase has a different gap structure compared with the NI phase. Let $\gamma = \frac{m_0 a^2}{2} > 0$. It is easy to show that for $J = 1$, if $\alpha \geq \alpha_c = -\frac{\epsilon_0^2}{2\gamma k_0^2}$, an energy gap of $2|\alpha|$ appears at $\mathbf{k} = (0, 0, \pm\frac{\pi}{a})$, whereas if $\alpha < \alpha_c$, a Mexican hat structure with the gap of $2\sqrt{2\alpha_c\alpha - \alpha_c^2}$ appears away from the \mathbf{k} point. Note that in addition to $(k_x, k_y, k_z) = (0, 0, \pm\frac{\pi}{a})$, there appear local minima at $(k_x, k_y, k_z) = (\pm\frac{\pi}{a}, 0, 0)$ and $(0, \pm\frac{\pi}{a}, 0)$ in the $J = 1$ 3D QAH phase, which result in an additional kink structure in the optical conductivity, as shown in Fig. 3(a) in the main text. For $J = 2$, there is always a Mexican hat structure for $\alpha < 0$ with a gap of $\frac{2|\alpha|}{\epsilon_0(\epsilon_0 + \Gamma)} \sqrt{\epsilon_0^2 \Gamma^2 + (\epsilon_0^2 + \epsilon_0 \Gamma - \Gamma^2)^2}$, where $\Gamma = \gamma k_0^2$.

D. Transition between the WSM and NI phases

At $m_z = t_z$, near $\mathbf{k} = (0, 0, 0)$, M_z can be approximated as

$$M_z \approx \frac{t_z a^2}{2} k_z^2 + \frac{m_0 a^2}{2} (k_x^2 + k_y^2). \quad (4)$$

Figure 4 shows the energy dispersion for the $J = 1$ and $J = 2$ lattice models at the transition between the WSM and NI phases. Note that the low-energy dispersion along the k_z direction with $k_x = k_y = 0$ is *quadratic*, while that along the k_x - k_y directions with $k_z = 0$ is linear for $J = 1$ and quadratic for $J > 1$. As shown in the main text, the change in energy dispersion affects the optical conductivity, exhibiting a different characteristic frequency dependence compared with that in the WSM or NI phase.

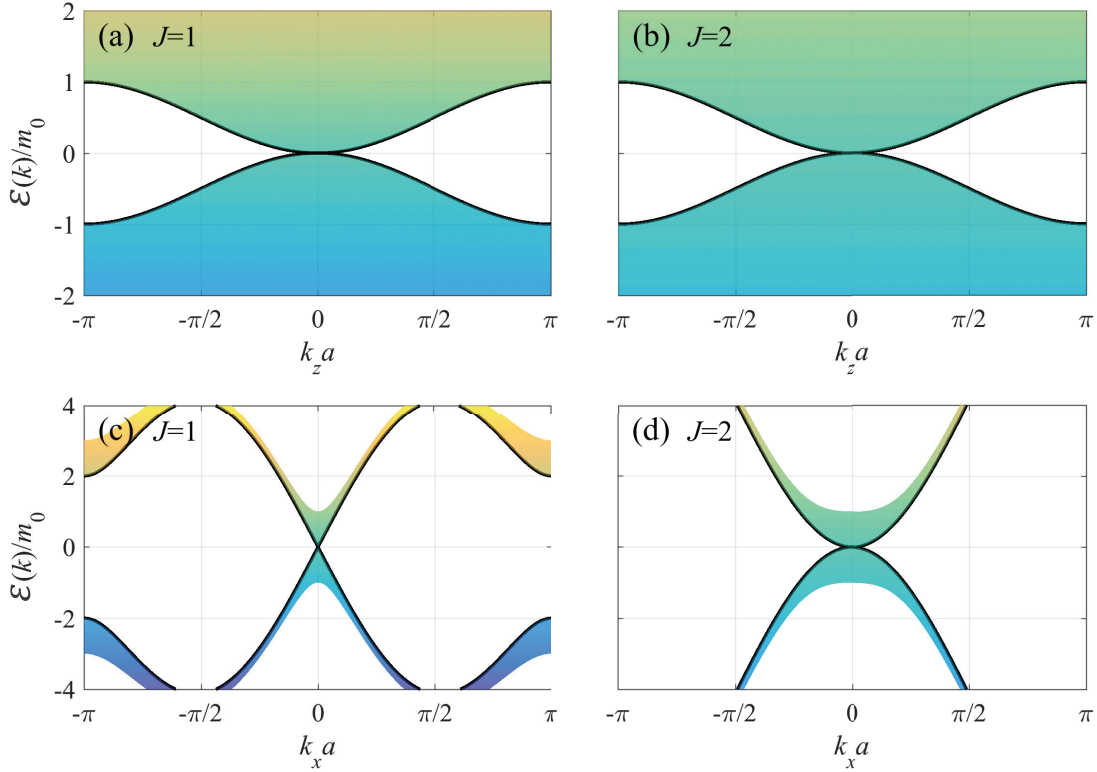


FIG. 4: Energy dispersions for the (a), (c) $J = 1$ and (b), (d) $J = 2$ lattice models at the transition between the WSM and NI phases viewed from the (a), (b) k_z - and (c), (d) k_x -axes with $k_y = 0$. Here, $m_z/m_0 = 0.5$ is used for the calculation.

E. Transition between the WSM and 3D QAH phases

At $m_z = -t_z$, near $\mathbf{k} = (0, 0, \pm \frac{\pi}{a})$, M_z can be approximated as

$$M_z \approx -\frac{t_z a^2}{2} q_z^2 + \frac{m_0 a^2}{2} (k_x^2 + k_y^2), \quad (5)$$

where $q_z = k_z \mp \frac{\pi}{a}$.

Figure 5 shows the energy dispersion for the $J = 1$ and $J = 2$ lattice models at the transition between the WSM and 3D QAH phases. Note that similar to the transition between the WSM and NI phases, the low-energy dispersion along the k_z direction with $k_x = k_y = 0$ is *quadratic*, while that along the k_x - k_y directions with $q_z = 0$ is linear for $J = 1$ and quadratic for $J > 1$. The change in energy dispersion affects the optical conductivity, exhibiting a different characteristic frequency dependence compared with that in the WSM or 3D QAH phase, as shown in Fig. 4 in the main text.

II. ANALYTIC EXPRESSIONS OF OPTICAL CONDUCTIVITY FOR EACH PHASE

In this section, we present detailed derivations of the optical conductivities for multi-Weyl semimetals in various phases. We consider the following continuum Hamiltonian introduced in Eq. (5) of the main text that describes various phases such as normal insulators (NIs), Weyl semimetals (WSM) and 3D quantum anomalous Hall (QAH) states, along with the transition between them:

$$H = \varepsilon_0 \left[\left(\frac{k_-}{k_0} \right)^J \sigma_+ + \left(\frac{k_+}{k_0} \right)^J \sigma_- \right] + M_z \sigma_z, \quad (6)$$

$$M_z = c_1 + c_2 \left(\frac{q_z}{k_0} \right)^n + c_3 \left[\left(\frac{k_x}{k_0} \right)^2 + \left(\frac{k_y}{k_0} \right)^2 \right],$$

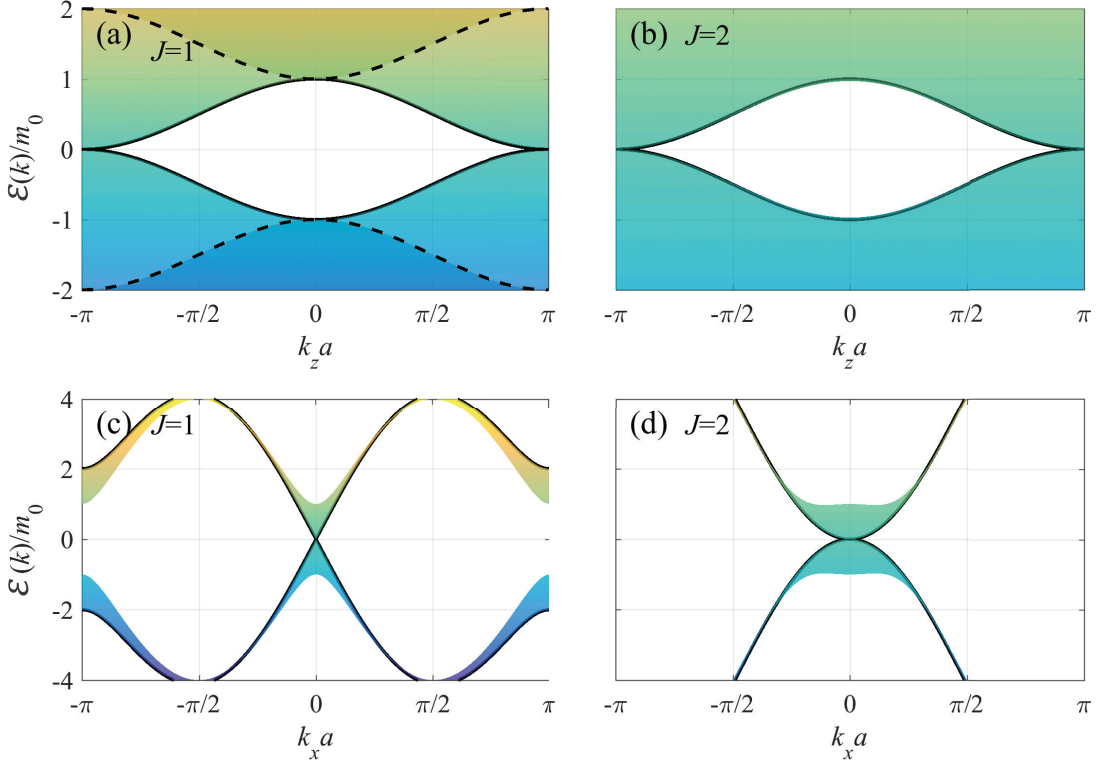


FIG. 5: Energy dispersions for the (a), (c) $J = 1$ and (b), (d) $J = 2$ lattice models at the transition between the WSM and 3D QAH phases viewed from the (a), (b) k_z - and (c), (d) k_x -axes with $k_y = 0$. Here, $m_z/m_0 = -0.5$ is used for the calculation.

where $\sigma_{\pm} = \frac{1}{2}(\sigma_x \pm i\sigma_y)$, $k_{\pm} = k_x \pm ik_y$, and q_z is the effective wavevector along the k_z direction defined in Eq. (6) of the main text. Note that for the WSM phase, $c_1 = 0$, $c_2 = \hbar v_z k_0$ and $c_3 = 0$ with $n = 1$, whereas for the insulator phases such as NI and 3D QAH, $c_1 = \alpha$, $c_2 = \beta k_0^2$ and $c_3 = \gamma k_0^2$ with $n = 2$. For the transition point, $c_1 = 0$, $c_2 = \beta k_0^2$ and $c_3 = \gamma k_0^2$ with $n = 2$.

A. Longitudinal optical conductivity

Using Eq. (7) in the main text, we can obtain optical conductivities for multi-Weyl semimetals in the non-interacting limit. Note that for the longitudinal conductivity, $M_i^{ss'}(\mathbf{k})M_i^{s's}(\mathbf{k}) = |M_i^{ss'}(\mathbf{k})|^2$ ($i = x, y, z$) is always real, thus the intraband and interband contributions of the real-part of the optical conductivity in the clean limit can be expressed as

$$\sigma_{ii}^{\text{intra}}(\omega) = -\frac{\pi e^2}{\hbar} \sum_{s=\pm} \int \frac{d^3k}{(2\pi)^3} \frac{\partial f_{s,\mathbf{k}}}{\partial \varepsilon_{s,\mathbf{k}}} |M_i^{ss}(\mathbf{k})|^2 \delta(\hbar\omega), \quad (7)$$

and

$$\sigma_{ii}^{\text{inter}}(\omega) = -\frac{\pi e^2}{\hbar} \int \frac{d^3k}{(2\pi)^3} \frac{f_{-,\mathbf{k}} - f_{+,\mathbf{k}}}{\varepsilon_{-,\mathbf{k}} - \varepsilon_{+,\mathbf{k}}} |M_i^{-+}(\mathbf{k})|^2 \delta(\hbar\omega + \varepsilon_{-,\mathbf{k}} - \varepsilon_{+,\mathbf{k}}), \quad (8)$$

at positive frequencies ($\omega > 0$).

Using this formula, it is straightforward to obtain the longitudinal optical conductivity for multi-Weyl semimetals. Because of the anisotropic energy dispersion, however, it is not trivial to obtain analytic expressions for the optical conductivity. In this section, we set $c_3 = 0$ (or $\gamma = 0$) for simplicity. This approximation works well for the Weyl phase because the linear term in M_z corresponding to the linear dispersion along the k_z direction is dominant over the quadratic mass term associated with γ at low frequencies. In the insulating phases, however, the linear term is absent, and thus neglecting the quadratic γ term is valid only when the effect of the band distortion associated with

nonzero γ is small ($m_0 \ll t_x, t_y$). [See Sec. III(a) for the effect of γ on the optical conductivity.] To avoid difficulties associated with anisotropic dispersions, we consider the following coordinate transformation

$$\begin{aligned} k_x &\rightarrow k_0 \left(\frac{\rho}{\varepsilon_0} \right)^{\frac{1}{J}} \cos \phi, \\ k_y &\rightarrow k_0 \left(\frac{\rho}{\varepsilon_0} \right)^{\frac{1}{J}} \sin \phi, \\ q_z &\rightarrow k_0 \left(\frac{z}{c_2} \right)^{\frac{1}{n}}, \end{aligned} \quad (9)$$

which transforms the Hamiltonian into the following linear form:

$$H = \rho(e^{-iJ\phi}\sigma_+ + e^{iJ\phi}\sigma_-) + (c_1 + z)\sigma_z. \quad (10)$$

Note that the transformed coordinates do not cover the lower hemisphere part (i.e., $q_z < 0$) when n is an even number. We can avoid this problem by taking advantage of the inversion symmetry of the system [$H(q_z) = H(-q_z)$ for even n], allowing us to get the right result by integrating over only the positive part of q_z . In the transformed coordinates, the energy dispersion is given by $E_{\pm}(\rho, z) = \pm E(\rho, z)$, where $E(\rho, z) = \sqrt{\rho^2 + (c_1 + z)^2}$. The corresponding eigenstate is given by

$$|+; \rho, \phi, z\rangle = \begin{pmatrix} \cos \frac{\theta}{2} \\ \sin \frac{\theta}{2} e^{iJ\phi} \end{pmatrix}, \quad (11a)$$

$$|-; \rho, \phi, z\rangle = \begin{pmatrix} -\sin \frac{\theta}{2} \\ \cos \frac{\theta}{2} e^{iJ\phi} \end{pmatrix}, \quad (11b)$$

where $\theta = \tan^{-1} \left(\frac{\rho}{c_1 + z} \right)$. Note that $\cos \theta = \frac{c_1 + z}{E(\rho, z)}$ and $\sin \theta = \frac{\rho}{E(\rho, z)}$.

The Jacobian \mathcal{J} corresponding to this transformation is given by

$$\mathcal{J} = \begin{vmatrix} \frac{\partial k_x}{\partial \rho} & \frac{\partial k_x}{\partial \phi} & \frac{\partial k_x}{\partial z} \\ \frac{\partial k_y}{\partial \rho} & \frac{\partial k_y}{\partial \phi} & \frac{\partial k_y}{\partial z} \\ \frac{\partial q_z}{\partial \rho} & \frac{\partial q_z}{\partial \phi} & \frac{\partial q_z}{\partial z} \end{vmatrix} = \frac{k_0^3 \left(\frac{\rho}{\varepsilon_0} \right)^{\frac{2}{J}} \left(\frac{z}{c_2} \right)^{\frac{1}{n}}}{Jn\rho z} \equiv \mathcal{J}(\rho, z). \quad (12)$$

The velocity matrices $\hat{v}_i = \frac{1}{\hbar} \frac{\partial \hat{H}}{\partial k_i}$ can be expressed as

$$\hat{v}_x = \frac{J\varepsilon_0}{\hbar k_0} \left(\frac{\rho}{\varepsilon_0} \right)^{\frac{J-1}{J}} \begin{pmatrix} 0 & e^{-i(J-1)\phi} \\ e^{i(J-1)\phi} & 0 \end{pmatrix}, \quad (13a)$$

$$\hat{v}_y = \frac{J\varepsilon_0}{\hbar k_0} \left(\frac{\rho}{\varepsilon_0} \right)^{\frac{J-1}{J}} \begin{pmatrix} 0 & -ie^{-i(J-1)\phi} \\ ie^{i(J-1)\phi} & 0 \end{pmatrix}, \quad (13b)$$

$$\hat{v}_z = \frac{nc_2}{\hbar k_0} \left(\frac{z}{c_2} \right)^{\frac{n-1}{n}} \begin{pmatrix} 1 & 0 \\ 0 & -1 \end{pmatrix}. \quad (13c)$$

Then, the matrix elements of $M_i^{ss'}(\mathbf{k}) = \langle s, \mathbf{k} | \hbar \hat{v}_i | s', \mathbf{k} \rangle$ used in $\sigma_{xx}(\omega)$ and $\sigma_{zz}(\omega)$ are given by

$$M_x^{++}(\mathbf{k}) = \frac{J\varepsilon_0}{k_0} \left(\frac{\rho}{\varepsilon_0} \right)^{\frac{J-1}{J}} \frac{\rho \cos \phi}{E(\rho, z)}, \quad (14a)$$

$$M_x^{-+}(\mathbf{k}) = \frac{J\varepsilon_0}{k_0} \left(\frac{\rho}{\varepsilon_0} \right)^{\frac{J-1}{J}} \left[\frac{c_1 + z}{E(\rho, z)} \cos \phi - i \sin \phi \right], \quad (14b)$$

$$M_z^{++}(\mathbf{k}) = \frac{nc_2}{k_0} \left(\frac{z}{c_2} \right)^{\frac{n-1}{n}} \frac{c_1 + z}{E(\rho, z)}, \quad (14c)$$

$$M_z^{-+}(\mathbf{k}) = -\frac{nc_2}{k_0} \left(\frac{z}{c_2} \right)^{\frac{n-1}{n}} \frac{\rho}{E(\rho, z)}. \quad (14d)$$

After integrating over ρ and ϕ in Eqs. (7) and (8), we can obtain the integral expressions with respect to z for the longitudinal optical conductivity. The intraband part at zero temperature for the chemical potential $\mu \geq 0$ is then given by

$$\begin{aligned}\sigma_{xx}^{\text{intra}}(\omega) &= \frac{\pi e^2}{\hbar} \int_{z_1}^{z_2} C_n dz \int_0^\infty d\rho \int_0^{2\pi} d\phi \frac{\mathcal{J}(\rho, z)}{(2\pi)^3} |M_x^{++}(\mathbf{k})|^2 \delta(\hbar\omega) \delta(\mu - E(\rho, z)) \\ &= \frac{\pi e^2}{\hbar} \delta(\hbar\omega) \int_{z_1}^{z_2} C_n dz \int_0^\infty d\rho \frac{\mathcal{J}(\rho, z)}{(2\pi)^2} \left(\frac{J\varepsilon_0}{k_0}\right)^2 \left(\frac{\rho}{\varepsilon_0}\right)^{\frac{2(J-1)}{J}} \frac{\rho^2}{2E^2(\rho, z)} \delta(\mu - E(\rho, z)) \\ &= \frac{e^2}{\hbar} \left(\frac{Jk_0\varepsilon_0^2}{8\pi n\mu}\right) \delta(\hbar\omega) \int_{z_1}^{z_2} C_n \frac{dz}{z} \left(\frac{z}{c_2}\right)^{\frac{1}{n}} \left(\frac{\rho_\mu(z)}{\varepsilon_0}\right)^2 \Theta(\mu - |c_1 + z|),\end{aligned}\quad (15a)$$

$$\begin{aligned}\sigma_{zz}^{\text{intra}}(\omega) &= \frac{\pi e^2}{\hbar} \int_{z_1}^{z_2} C_n dz \int_0^\infty d\rho \int_0^{2\pi} d\phi \frac{\mathcal{J}(\rho, z)}{(2\pi)^3} |M_z^{++}(\mathbf{k})|^2 \delta(\hbar\omega) \delta(\mu - E(\rho, z)) \\ &= \frac{\pi e^2}{\hbar} \delta(\hbar\omega) \int_{z_1}^{z_2} C_n dz \int_0^\infty d\rho \frac{\mathcal{J}(\rho, z)}{(2\pi)^2} \left(\frac{nc_2}{k_0}\right)^2 \left(\frac{z}{c_2}\right)^{\frac{2(n-1)}{n}} \frac{(c_1 + z)^2}{E^2(\rho, z)} \delta(\mu - E(\rho, z)) \\ &= \frac{e^2}{\hbar} \left(\frac{nk_0c_2^2}{4\pi J\mu}\right) \delta(\hbar\omega) \int_{z_1}^{z_2} C_n \frac{dz}{z} \left(\frac{z}{c_2}\right)^{\frac{2n-1}{n}} \left(\frac{c_1 + z}{\varepsilon_0}\right)^2 \left(\frac{\rho_\mu(z)}{\varepsilon_0}\right)^{\frac{2(1-J)}{J}} \Theta(\mu - |c_1 + z|),\end{aligned}\quad (15b)$$

where $\rho_\mu(z) = \sqrt{\mu^2 - (c_1 + z)^2}$ and $\Theta(x)$ is the step function with $\Theta(x) = 1$ for $x > 0$ and 0 otherwise. The integration range is $(z_1, z_2) = (-\infty, \infty)$ for odd n , $(z_1, z_2) = (0, \infty)$ for even n and $c_2 > 0$, and $(z_1, z_2) = (-\infty, 0)$ for even n and $c_2 < 0$, and $C_n = 2$ for even n and $C_n = 1$ for odd n . Here for the ρ integration with a delta function, we use the relation $\delta(f(\rho)) = \frac{1}{|f'(\rho_0)|} \delta(\rho - \rho_0)$, where $f(\rho_0) = 0$.

For the interband part of optical conductivity, we set $\mu = 0$ for simplicity. Note that non-zero μ at zero temperature only gives rise to the Pauli blocking effect, thus the effect of non-zero μ can be taken into account by introducing the step function $\Theta(\hbar\omega - 2|\mu|)$ into the $\mu = 0$ result. [See Sec. III(c) for further discussion on the effect of finite μ .] The interband part at zero temperature with $\mu = 0$ is given by

$$\begin{aligned}\sigma_{xx}^{\text{inter}}(\omega) &= \frac{\pi e^2}{\hbar} \int_{z_1}^{z_2} C_n dz \int_0^\infty d\rho \int_0^{2\pi} d\phi \frac{\mathcal{J}(\rho, z)}{(2\pi)^3} \frac{|M_x^{-+}(\mathbf{k})|^2}{2E(\rho, z)} \delta(\hbar\omega - 2E(\rho, z)) \\ &= \frac{\pi e^2}{\hbar} \int_{z_1}^{z_2} C_n dz \int_0^\infty d\rho \frac{\mathcal{J}(\rho, z)}{(2\pi)^2} \frac{1}{2E(\rho, z)} \left(\frac{J\varepsilon_0}{k_0}\right)^2 \left(\frac{\rho}{\varepsilon_0}\right)^{\frac{2(J-1)}{J}} \frac{1}{2} \left[\frac{(c_1 + z)^2}{E^2(\rho, z)} + 1\right] \delta(\hbar\omega - 2E(\rho, z)) \\ &= \frac{e^2}{\hbar} \left(\frac{Jk_0}{32\pi n}\right) \int_{z_1}^{z_2} C_n \frac{dz}{z} \left(\frac{z}{c_2}\right)^{\frac{1}{n}} \left[\frac{(c_1 + z)^2}{(\hbar\omega/2)^2} + 1\right] \Theta\left(\frac{\hbar\omega}{2} - |c_1 + z|\right),\end{aligned}\quad (16a)$$

$$\begin{aligned}\sigma_{zz}^{\text{inter}}(\omega) &= \frac{\pi e^2}{\hbar} \int_{z_1}^{z_2} C_n dz \int_0^\infty d\rho \int_0^{2\pi} d\phi \frac{\mathcal{J}(\rho, z)}{(2\pi)^3} \frac{|M_z^{-+}(\mathbf{k})|^2}{2E(\rho, z)} \delta(\hbar\omega - 2E(\rho, z)) \\ &= \frac{\pi e^2}{\hbar} \int_{z_1}^{z_2} C_n dz \int_0^\infty d\rho \frac{\mathcal{J}(\rho, z)}{(2\pi)^2} \frac{1}{2E(\rho, z)} \left(\frac{nc_2}{k_0}\right)^2 \left(\frac{z}{c_2}\right)^{\frac{2(n-1)}{n}} \frac{\rho^2}{E^2(\rho, z)} \delta(\hbar\omega - 2E(\rho, z)) \\ &= \frac{e^2}{\hbar} \left(\frac{nk_0}{4\pi J}\right) \left(\frac{c_2}{\hbar\omega}\right)^2 \int_{z_1}^{z_2} C_n \frac{dz}{z} \left(\frac{z}{c_2}\right)^{\frac{2n-1}{n}} \left(\frac{\rho_\omega(z)}{\varepsilon_0}\right)^{\frac{2}{J}} \Theta\left(\frac{\hbar\omega}{2} - |c_1 + z|\right),\end{aligned}\quad (16b)$$

where $\rho_\omega(z) = \sqrt{(\hbar\omega/2)^2 - (c_1 + z)^2}$. In the subsequent sections, we present calculated optical conductivity for each phase.

1. WSM phase

For the WSM phase, $c_1 = 0$, $c_2 = \hbar v_z k_0$, $c_3 = 0$ and $n = 1$. From Eqs. (15) and (16), the longitudinal optical conductivity is given by

$$\sigma_{xx}(\omega) = \frac{g_N}{24\pi} \frac{J e^2}{\hbar v_z} [\omega \Theta(\hbar\omega - 2|\mu|) + 4\omega_\mu^2 \delta(\omega)], \quad (17a)$$

$$\sigma_{zz}(\omega) = \frac{g_N}{24\pi} \frac{e^2 v_z}{\hbar v_z^2} \left[A_{zz}^{\text{WSM}} \left(\frac{\omega}{\omega_0} \right)^{\frac{2}{J}-1} \omega_0 \Theta(\hbar\omega - 2|\mu|) + 4B_{zz}^{\text{WSM}} \left(\frac{|\omega_\mu|}{\omega_0} \right)^{\frac{2}{J}} \omega_0^2 \delta(\omega) \right], \quad (17b)$$

where $\varepsilon_0 = \hbar\omega_0 = \hbar v_{\parallel} k_0$, $\omega_\mu \equiv \mu/\hbar$, $A_{zz}^{\text{WSM}} = \frac{3\sqrt{\pi}\Gamma(\frac{1}{J})}{2^{\frac{2}{J}} J^2 \Gamma(\frac{1}{J} + \frac{3}{2})}$, and $B_{zz}^{\text{WSM}} = \frac{3\sqrt{\pi}\Gamma(\frac{1}{J})}{4J\Gamma(\frac{1}{J} + \frac{3}{2})}$. Here, we introduced the number of nodes g_N . In the derivation for σ_{zz} , we substitute $\frac{z}{\mu} = \sin\theta$ or $\frac{z}{\hbar\omega/2} = \sin\theta$, and use the relation $\int_0^{\pi/2} d\theta \cos^m \theta \sin^n \theta = \frac{1}{2} B(\frac{m+1}{2}, \frac{n+1}{2})$ where $B(m, n) = \frac{\Gamma(m)\Gamma(n)}{\Gamma(m+n)}$ is the beta function and $\Gamma(x) = \int_0^\infty dt t^{x-1} e^{-t}$ is the gamma function (See Ref. 18 in the main text.) Note that for $J = 1$, $A_{zz}^{\text{WSM}}|_{J=1} = B_{zz}^{\text{WSM}}|_{J=1} = 1$ and the result in Eq. (17) reduces to that of conventional Weyl semimetals.

The first term in Eq. (17) represents the interband transitions, which are forbidden at $\omega < 2|\omega_\mu|$ due to Pauli blocking, whereas the second term represents the intraband transition giving rise to the Drude peak at low frequencies. For the undoped case ($\mu = 0$), the result reduces to Eq. (8) in the main text.

2. Insulator phase

For both the NI and 3D QAH phases, $c_1 = \alpha$, $c_2 = \beta k_0^2$ and $n = 2$. As discussed, we set $c_3 = 0$ (or $\gamma = 0$) for simplicity. From now on, we consider only the undoped case, $\mu = 0$. The longitudinal optical conductivity is then obtained to be

$$\sigma_{xx}(\omega) = \frac{e^2}{\hbar} G_{xx}(\omega) (\hbar\omega - 2|\alpha|)^{\frac{1}{2}} \Theta(\hbar\omega - 2|\alpha|), \quad (18a)$$

$$\sigma_{zz}(\omega) = \frac{e^2}{\hbar} G_{zz}(\omega) (\hbar\omega - 2|\alpha|)^{\frac{1}{J} + \frac{3}{2}} \Theta(\hbar\omega - 2|\alpha|), \quad (18b)$$

where

$$G_{xx}(\omega) = \frac{J (16|\alpha|^2 + 4|\alpha|\hbar\omega + 9(\hbar\omega)^2)}{120\sqrt{2}\pi|\beta|^{\frac{1}{2}}(\hbar\omega)^2}, \quad (19a)$$

$$G_{zz}(\omega) = \frac{k_0\Gamma(\frac{1}{J})}{2^{\frac{2}{J} + \frac{5}{2}}\sqrt{\pi}J^2\Gamma(\frac{1}{J} + \frac{5}{2})} \frac{(|\beta|k_0^2)^{\frac{1}{2}}(\hbar\omega + 2|\alpha|)^{\frac{1}{J}}}{\varepsilon_0^{\frac{2}{J}}(\hbar\omega)^2} {}_2F_1\left(-\frac{1}{J}, \frac{3}{2}; \frac{1}{J} + \frac{5}{2}; \frac{2|\alpha| - \hbar\omega}{2|\alpha| + \hbar\omega}\right), \quad (19b)$$

and ${}_2F_1(a, b; c; z) = \frac{\Gamma(c)}{\Gamma(b)\Gamma(c-b)} \int_0^1 dt \frac{t^{b-1}(1-t)^{c-b-1}}{(1-tz)^a}$ is the hypergeometric function. Note that the analytic expressions for the longitudinal conductivities with $\gamma = 0$ have the same form for both NI and 3D QAH phases except for the sign of α : $\alpha > 0$ for the NI phase and $\alpha < 0$ for the 3D QAH phase.

3. Transition point

For the transition point between the WSM and NI phases or between the WSM and 3D QAH phases, the analytical results can be obtained by taking the limit $\alpha \rightarrow 0$ in Eq. (18):

$$\sigma_{xx}(\omega) = \frac{e^2}{\hbar} A_{xx}(\hbar\omega)^{\frac{1}{2}}, \quad (20a)$$

$$\sigma_{zz}(\omega) = \frac{e^2}{\hbar} A_{zz}(\hbar\omega)^{\frac{2}{J} - \frac{1}{2}}, \quad (20b)$$

where

$$A_{xx} = \frac{3J}{40\sqrt{2\pi}|\beta|^{\frac{1}{2}}}, \quad (21a)$$

$$A_{zz} = \frac{k_0\Gamma\left(\frac{1}{J}\right)(|\beta|k_0^2)^{\frac{1}{2}}}{2^{\frac{2}{J}+2}J^2\Gamma\left(\frac{1}{4}\right)\Gamma\left(\frac{1}{J}+\frac{7}{4}\right)\varepsilon_0^{\frac{2}{J}}}. \quad (21b)$$

Here, we used ${}_2F_1(a, b; c; z) = {}_2F_1(b, a; c; z)$, ${}_2F_1(a, b; 1+a-b; -1) = \frac{\Gamma(1+a-b)\Gamma(1+\frac{1}{2}a)}{\Gamma(1+a)\Gamma(1+\frac{1}{2}a-b)}$, and $\Gamma(x)\Gamma(1-x) = \frac{\pi}{\sin \pi x}$. (See Ref. 18 in the main text.)

B. Transverse optical conductivity

From Eq. (7) in the main text, the Hall or transverse optical conductivity σ_{xy} for $\mu = 0$ is given by

$$\sigma_{xy}(\omega) = -\frac{ie^2}{\hbar} \int \frac{d^3k}{(2\pi)^3} \frac{f_{+, \mathbf{k}} - f_{-, \mathbf{k}}}{\varepsilon_{+, \mathbf{k}} - \varepsilon_{-, \mathbf{k}}} \left[\frac{M_x^{+-}(\mathbf{k})M_y^{-+}(\mathbf{k})}{\hbar\omega + \varepsilon_{+, \mathbf{k}} - \varepsilon_{-, \mathbf{k}}} + \frac{M_x^{-+}(\mathbf{k})M_y^{+-}(\mathbf{k})}{\hbar\omega + \varepsilon_{-, \mathbf{k}} - \varepsilon_{+, \mathbf{k}}} \right]. \quad (22)$$

Here, in contrast to the longitudinal optical conductivity, we keep c_3 (or γ) for analytic expressions. Throughout this section, for brevity, the momentum and the energy are normalized by k_0 and ε_0 , respectively, or equivalently we set $k_0 = \varepsilon_0 = 1$.

We consider the following coordinate transformation:

$$\begin{aligned} k_x &\rightarrow \rho^{\frac{1}{J}} \cos \phi, \\ k_y &\rightarrow \rho^{\frac{1}{J}} \sin \phi, \\ k_z &\rightarrow k_z, \end{aligned} \quad (23)$$

whose Jacobian is given by

$$\mathcal{J} = \frac{\rho^{\frac{2}{J}-1}}{J} \equiv \mathcal{J}(\rho). \quad (24)$$

In the transformed coordinate, the Hamiltonian becomes

$$H = \rho(e^{-iJ\phi}\sigma_+ + e^{iJ\phi}\sigma_-) + (c_1 + c_2q_z^n + c_3\rho^{\frac{2}{J}})\sigma_z, \quad (25)$$

and the energy dispersion is given by $E_{\pm}(\rho, q_z) = \pm E(\rho, q_z)$, where

$$E(\rho, q_z) = \sqrt{\rho^2 + \left(c_1 + c_2q_z^n + c_3\rho^{\frac{2}{J}}\right)^2}. \quad (26)$$

The corresponding eigenstate is given by

$$|+; \rho, \phi, q_z\rangle = \begin{pmatrix} \cos \frac{\theta}{2} \\ \sin \frac{\theta}{2} e^{iJ\phi} \end{pmatrix}, \quad (27a)$$

$$|-; \rho, \phi, q_z\rangle = \begin{pmatrix} -\sin \frac{\theta}{2} \\ \cos \frac{\theta}{2} e^{iJ\phi} \end{pmatrix}, \quad (27b)$$

where $\theta = \tan^{-1}\left(\frac{\rho}{m(\rho, q_z)}\right)$ and $m(\rho, q_z) = c_1 + c_2q_z^n + c_3\rho^{\frac{2}{J}}$. Note that $\cos \theta = \frac{m(\rho, q_z)}{E(\rho, q_z)}$ and $\sin \theta = \frac{\rho}{E(\rho, q_z)}$.

The velocity matrices $\hat{v}_i = \frac{1}{\hbar} \frac{\partial \hat{H}}{\partial k_i}$ can be expressed as

$$\hat{v}_x = \frac{1}{\hbar} \begin{pmatrix} 2c_3\rho^{\frac{1}{J}} \cos \phi & J\rho^{\frac{J-1}{J}} e^{-i(J-1)\phi} \\ J\rho^{\frac{J-1}{J}} e^{i(J-1)\phi} & -2c_3\rho^{\frac{1}{J}} \cos \phi \end{pmatrix}, \quad (28a)$$

$$\hat{v}_y = \frac{1}{\hbar} \begin{pmatrix} 2c_3\rho^{\frac{1}{J}} \sin \phi & -iJ\rho^{\frac{J-1}{J}} e^{-i(J-1)\phi} \\ iJ\rho^{\frac{J-1}{J}} e^{i(J-1)\phi} & -2c_3\rho^{\frac{1}{J}} \sin \phi \end{pmatrix}. \quad (28b)$$

Then the matrix elements of $M_i^{ss'}(\mathbf{k}) = \langle s, \mathbf{k} | \hat{h}v_i | s', \mathbf{k} \rangle$ used in $\sigma_{xy}(\omega)$ are given by

$$M_x^{+-}(\mathbf{k}) = J \left[\rho^{\frac{J-1}{J}} (\cos \theta \cos \phi + i \sin \phi) \right] - 2c_3 \rho^{\frac{1}{J}} \sin \theta \cos \phi, \quad (29a)$$

$$M_y^{-+}(\mathbf{k}) = J \left[\rho^{\frac{J-1}{J}} (\cos \theta \sin \phi + i \cos \phi) \right] - 2c_3 \rho^{\frac{1}{J}} \sin \theta \sin \phi. \quad (29b)$$

Note that

$$\int_0^{2\pi} \frac{d\phi}{2\pi} M_x^{+-}(\mathbf{k}) M_y^{-+}(\mathbf{k}) = \int_0^{2\pi} \frac{d\phi}{2\pi} (M_x^{-+}(\mathbf{k}) M_y^{+-}(\mathbf{k}))^* = iJ^2 \rho^{\frac{2(J-1)}{J}} \left[\frac{J(c_1 + c_2 q_z^n) + (J-2)c_3 \rho^{\frac{2}{J}}}{E(\rho, q_z)} \right]. \quad (30)$$

Then, from Eq. (22) the real part of the transverse optical conductivity is given by

$$\begin{aligned} \sigma_{xy}(\omega) &= -\frac{ie^2}{\hbar} \int_0^\infty d\rho \int_{-k_c}^{k_c} dk_z \int_0^{2\pi} d\phi \frac{\mathcal{J}(\rho)}{(2\pi)^3} \frac{1}{2E(\rho, q_z)} \left[\frac{M_x^{+-}(\mathbf{k}) M_y^{-+}(\mathbf{k})}{\hbar\omega + 2E(\rho, q_z)} + \frac{M_x^{-+}(\mathbf{k}) M_y^{+-}(\mathbf{k})}{\hbar\omega - 2E(\rho, q_z)} \right] \\ &= -\frac{e^2}{\hbar} \frac{1}{8\pi^2} \int_0^\infty \rho d\rho \int_{-k_c}^{k_c} dk_z \left[\frac{J(c_1 + c_2 q_z^n) + (J-2)c_3 \rho^{\frac{2}{J}}}{E(\rho, q_z)} \right] \left[\frac{1}{E^2(\rho, q_z) - (\hbar\omega/2)^2} \right]. \end{aligned} \quad (31)$$

Here, we introduce the momentum cutoff k_c along the k_z direction to prevent divergence of the integral. Using these results, we can obtain the real part of the transverse optical conductivity up to second order in ω as $\sigma_{xy}(\omega) \approx \sigma_{xy}^{(0)} + \sigma_{xy}^{(2)}(\omega)$, where

$$\begin{aligned} \sigma_{xy}^{(0)} &= -\frac{e^2}{\hbar} \frac{1}{8\pi^2} \int_{-k_c}^{k_c} dk_z \int_0^\infty \rho d\rho \frac{J(c_1 + c_2 q_z^n) + (J-2)c_3 \rho^{\frac{2}{J}}}{E^3(\rho, q_z)} \\ &= \frac{e^2}{\hbar} \frac{1}{8\pi^2} \int_{-k_c}^{k_c} dk_z \frac{J(c_1 + c_2 q_z^n + c_3 \rho^{\frac{2}{J}})}{E(\rho, q_z)} \Bigg|_{\rho \rightarrow 0}^{\rho \rightarrow \infty}, \end{aligned} \quad (32a)$$

$$\sigma_{xy}^{(2)}(\omega) = -\frac{e^2}{\hbar} \frac{(\hbar\omega)^2}{32\pi^2} \int_{-k_c}^{k_c} dk_z \int_0^\infty \rho d\rho \frac{J(c_1 + c_2 q_z^n) + (J-2)c_3 \rho^{\frac{2}{J}}}{E^5(\rho, q_z)}. \quad (32b)$$

From now on, we recover k_0 and ε_0 for clarity.

1. WSM phase

For the WSM phase, $c_1 = 0$, $c_2 = \hbar v_z k_0$, $c_3 = 0$ and $n = 1$. Then the Hall conductivity for a single Weyl node is given by

$$\sigma_{xy}^{(0)} = -\frac{e^2}{\hbar} \frac{J}{8\pi^2} \int_{-k_c}^{k_c} dk_z \text{sgn}(v_z q_z). \quad (33)$$

Note that there always appear multiple Weyl points in the Brillouin zone with the total chirality summing to zero. Here, we consider the simplest case in which two Weyl nodes with opposite chirality are located at $\pm b\hat{z}$, respectively. Assuming that the node with positive chirality is at $k_z = +b\hat{z}$ and the negative one is at $k_z = -b\hat{z}$ with $|b| < k_c$, we find

$$\sigma_{xy}^{(0)} = -\frac{e^2}{\hbar} \frac{J}{8\pi^2} \int_{-k_c}^{k_c} dk_z \{ \text{sgn}[v_z(k_z - b)] + \text{sgn}[(-v_z)(k_z + b)] \} \quad (34)$$

$$= J \frac{e^2}{\hbar} \frac{b}{\pi}. \quad (35)$$

Here, the first and second terms in the first line represent contributions from the positive and negative chirality nodes, respectively.

Similarly, we can obtain the dynamical part of the Hall conductivity. For a single Weyl node,

$$\begin{aligned} \sigma_{xy}^{(2)}(\omega) &= -\frac{e^2}{\hbar} \frac{J(\hbar\omega)^2}{32\pi^2} \int_{-k_c}^{k_c} dk_z \int_0^\infty \rho d\rho \frac{\hbar v_z q_z}{[\rho^2 + (\hbar v_z q_z)^2]^{\frac{5}{2}}} \\ &= -\frac{e^2}{\hbar} \frac{J(\hbar\omega)^2}{96\pi^2} \int_{-k_c}^{k_c} dk_z \frac{\text{sgn}(v_z q_z)}{(\hbar v_z q_z)^2}. \end{aligned} \quad (36)$$

Then, the total conductivity contributed from the two Weyl nodes is given by

$$\begin{aligned}\sigma_{xy}^{(2)}(\omega) &= -\frac{e^2}{\hbar} \frac{J\omega^2}{96\pi^2 v_z^2} \int_{-k_c}^{k_c} dk_z \left\{ \frac{\text{sgn}[v_z(k_z - b)]}{(k_z - b)^2} + \frac{\text{sgn}[(-v_z)(k_z + b)]}{(k_z + b)^2} \right\} \\ &= \frac{e^2}{\hbar} \frac{J}{24\pi^2 v_z^2} \frac{b}{k_c^2 - b^2} \omega^2.\end{aligned}\quad (37)$$

2. Insulator phase

For both the NI and 3D QAH phases, $c_1 = \alpha$, $c_2 = \beta k_0^2$, $c_3 = \gamma k_0^2$ and $n = 2$. The static part of the Hall conductivity after the integration over ρ is given by

$$\sigma_{xy}^{(0)} = \frac{e^2}{\hbar} \frac{1}{8\pi^2} \int_{-k_c}^{k_c} dk_z \begin{cases} 1 - \text{sgn}[f(q_z)] & (J = 1), \\ \frac{2\gamma k_0^2}{\sqrt{(\gamma k_0^2)^2 + \varepsilon_0^2}} - 2\text{sgn}[f(q_z)] & (J = 2), \end{cases}\quad (38)$$

where $f(q_z) = \alpha + \beta q_z^2$. Now, the integral is straightforward. In the NI phase ($\alpha > 0$, $\beta > 0$), $\text{sgn}[f(q_z)] = 1$, thus

$$\sigma_{xy}^{(0)} = \frac{e^2}{\hbar} \begin{cases} 0 & (J = 1), \\ \frac{k_c}{2\pi^2} \left(\frac{\gamma k_0^2}{\sqrt{(\gamma k_0^2)^2 + \varepsilon_0^2}} - 1 \right) & (J = 2), \end{cases}\quad (39)$$

whereas in the 3D QAH phase ($\alpha < 0$, $\beta < 0$), $\text{sgn}[f(q_z)] = -1$, and so

$$\sigma_{xy}^{(0)} = \frac{e^2}{\hbar} \begin{cases} \frac{k_c}{2\pi^2} & (J = 1), \\ \frac{k_c}{2\pi^2} \left(\frac{\gamma k_0^2}{\sqrt{(\gamma k_0^2)^2 + \varepsilon_0^2}} + 1 \right) & (J = 2). \end{cases}\quad (40)$$

The results in Eq. (39) show that the static Hall conductivity $\sigma_{xy}^{(0)}$ in the NI phase is nonzero for $J = 2$ in contrast to the corresponding lattice result, and that $\sigma_{xy}^{(0)}$ for the $J = 2$ 3D QAH phase in Eq. (40) contains material dependent parameters such as γ and ε_0 . This is puzzling because the static Hall conductivity characterizing the topological state of the system should have a quantized value. The reason is that the static Hall conductivity for the continuum model is not properly regularized carrying an arbitrary residual value, thus it is not directly experimentally measurable but the difference in this quantity between different electronic states is. Since we know that the static part of the Hall conductivity in the NI phase is necessarily zero, we can directly obtain the residual conductivity to be $\sigma_{xy}^{(0)}$ in the NI phase. It is important to note that for the $J = 2$ 3D QAH phase, after subtracting the residual conductivity, we obtain $\sigma_{xy}^{(0)} \Big|_{\text{QAH}} \rightarrow \sigma_{xy}^{(0)} \Big|_{\text{QAH}} - \sigma_{xy}^{(0)} \Big|_{\text{NI}} = \frac{2e^2}{\hbar} \frac{k_c}{2\pi^2}$, as in Eq. (10) in the main text, which is quantized and consistent with the

lattice result. (In general, the static Hall conductivity is proportional to the chirality so that $\sigma_{xy}^{(0)} \Big|_{\text{QAH}} \rightarrow \frac{J e^2}{\hbar} \frac{k_c}{2\pi^2}$.)

Note that the continuum model Hall conductivities presented in the figures throughout the paper (both numerical and analytic results) have this residual conductivity subtracted. In this sense, we choose the momentum cutoff along the k_z direction as $k_c = \pi/a$ so that the properly subtracted static Hall conductivity in the 3D QAH phase has the same quantized value as in the lattice model.

Similarly, we can obtain the dynamical part of the Hall conductivity, whose leading order contribution is quadratic in frequency, i.e., $\sigma_{xy}^{(2)} = \frac{e^2}{\hbar} B_{xy} \omega^2$. In the NI phase,

$$B_{xy}^{\text{NI}} = k_0 \left(\frac{\hbar}{\varepsilon_0} \right)^2 \begin{cases} -\frac{k_c \varepsilon_0^2}{96\pi^2 \alpha k_0 (\alpha + \beta k_c^2)} + \frac{8\alpha \gamma k_0^2 - \varepsilon_0^2}{96\pi^2 \sqrt{\alpha^3 \beta} k_0} \tan^{-1} \left(\sqrt{\frac{\beta}{\alpha}} k_c \right) - \frac{\gamma k_0^2 \tan^{-1} \left[2\sqrt{\frac{\beta k_c^2 \gamma k_0^2}{4\alpha \gamma k_0^2 + \varepsilon_0^2}} \right]}{6\pi^2 \sqrt{\frac{\beta(4\alpha \gamma k_0^2 + \varepsilon_0^2)}{\gamma}}} & (J = 1), \\ \frac{\gamma k_0^2 \varepsilon_0}{24\pi^2 \alpha^2 (\alpha + \beta k_c^2)} \sqrt{\frac{\alpha(\gamma^2 k_0^4 + \varepsilon_0^2)}{\beta k_0^2 \varepsilon_0^2}} \left[\tan^{-1} \left(\sqrt{\frac{\beta}{\alpha}} k_c \right) (\alpha + \beta k_c^2) - k_c \sqrt{\alpha \beta} \right] & (J = 2), \end{cases}\quad (41)$$

whereas in the 3D QAH phase,

$$B_{xy}^{\text{QAH}} = k_0 \left(\frac{\hbar}{\varepsilon_0} \right)^2 \begin{cases} \frac{k_c \varepsilon_0^2}{96\pi^2 k_0 \alpha (\alpha + \beta k_c^2)} - \frac{8\alpha \gamma k_0^2 - \varepsilon_0^2}{96\pi^2 \sqrt{\alpha^3 \beta} k_0} \tan^{-1} \left(\sqrt{\frac{\beta}{\alpha}} k_c \right) & (J = 1), \\ \frac{\gamma k_0^2 \varepsilon_0}{24\pi^2 \alpha^2 (\alpha + \beta k_c^2)} \sqrt{\frac{\alpha(\gamma^2 k_0^4 + \varepsilon_0^2)}{\beta k_0^2 \varepsilon_0^2}} \left[\tan^{-1} \left(\sqrt{\frac{\beta}{\alpha}} k_c \right) (\alpha + \beta k_c^2) - k_c \sqrt{\alpha \beta} \right] & (J = 2). \end{cases}\quad (42)$$

Note that for $J = 2$, the dynamical part for the 3D QAH phase is given by the same form as that for the NI phase. In addition, B_{xy}^{NI} and B_{xy}^{QAH} are not zero, indicating that the system is a dynamical Hall insulator, even in the NI phase. Deep inside the NI (3D QAH) phase, however, $\lim_{\alpha \rightarrow \pm\infty} B_{xy} = 0$, thus the system becomes a trivial insulator (quantized Hall insulator) at finite frequencies.

3. Transition point

For the transition point between the NI and WSM phases or between the 3D QAH and WSM phases, $c_1 = 0$, $c_2 = \beta k_0^2$, $c_3 = \gamma k_0^2$ and $n = 2$. Then, the transverse optical conductivity is given by the following form:

$$\sigma_{xy}^{\text{NI|WSM}}(\omega) = \frac{e^2}{\hbar} [A_{xy}^{\text{NI}} + C_{xy}^{\text{NI|WSM}} \omega^\nu], \quad (43a)$$

$$\sigma_{xy}^{\text{QAH|WSM}}(\omega) = \frac{e^2}{\hbar} \left[\frac{Jk_c}{2\pi^2} + A_{xy}^{\text{NI}} + C_{xy}^{\text{QAH|WSM}} \omega^\nu \right], \quad (43b)$$

where A_{xy}^{NI} is a residual conductivity for the NI phase given by $A_{xy}^{\text{NI}}|_{J=1} = 0$ for $J = 1$ and $A_{xy}^{\text{NI}}|_{J=2} = \frac{k_c}{2\pi^2} \left(\frac{\gamma k_0^2}{\sqrt{(\gamma k_0^2)^2 + \varepsilon_0^2}} - 1 \right)$ for $J = 2$, as shown in Eq. (39). As discussed in Sec. II B 2, the residual term A_{xy}^{NI} should be subtracted for the proper regularization, as shown in Eq. (11c) in the main text. Here, the exponent $\nu \approx 0.5$ is found numerically from Eq. (31) for $J = 1, 2$ with frequency independent coefficients $C_{xy}^{\text{NI|WSM}}$ and $C_{xy}^{\text{QAH|WSM}}$, respectively.

III. EFFECTS OF THE γ TERM, IMPURITIES, CHEMICAL POTENTIAL AND TILT ON THE OPTICAL CONDUCTIVITY

In this section, we discuss the effects of γ , impurities, chemical potential, and tilt on the optical conductivity, focusing on the validity of the characteristic frequency dependence described in this work. We show that the characteristic frequency dependence described in the main text is not altered below the frequency corresponding to the energy scale of the tilt or impurity potential. Here, we limit our discussion to the range of frequencies below the energy scale that the lattice effect becomes important and the Weyl Hamiltonian is no longer valid.

A. γ term

In the main text, we obtained the power-law in the longitudinal optical conductivities assuming $\gamma = 0$ in the insulating phases [Eq. (9) in the main text] and at the transition point [Eq. (11) in the main text]. Figure 6 shows the deviation of the power-law from that obtained within the $\gamma = 0$ approximation in the NI phase. For $J = 1$, the power-law is robust against the increase of γ because the linear in-plane energy dispersion dominates over the quadratic term associated with γ . For $J = 2$, however, the deviation of the power-law is significant because the quadratic in-plane energy dispersion is comparable to the quadratic γ term. At the transition point between the NI and WSM phases, the power-law is barely altered by γ for both $J = 1$ and $J = 2$. The same conclusion holds for the QAH phase and the transition point between the QAH and WSM phases, because the gapped band structure is similar to that of the NI phase, unless a Mexican hat structure appears. Thus, we find that the deviation from the $\gamma = 0$ approximation is significant in the gapped phases for $J = 2$ but not in the gapless phases which extend to low frequency.

B. Impurities

The effect of impurities or disorder can be taken into account in a simple form as a finite broadening term η replacing the 0^+ term in Eq. (6) in the main text for the Kubo formula. Figure 7 shows calculated optical conductivities for several values of η which characterizes the strength of the impurity potential. Impurities affect the power-law in the optical conductivity below the frequency range set by the energy scale of the impurity potential. Above this energy scale, however, the characteristic power-law obtained in the clean limit remains valid. Note that simulating impurity effects with a broadening η is approximate, and strong enough disorder can induce a phase transition, as shown in Ref. 12 in the main text, which is beyond the scope of this work.

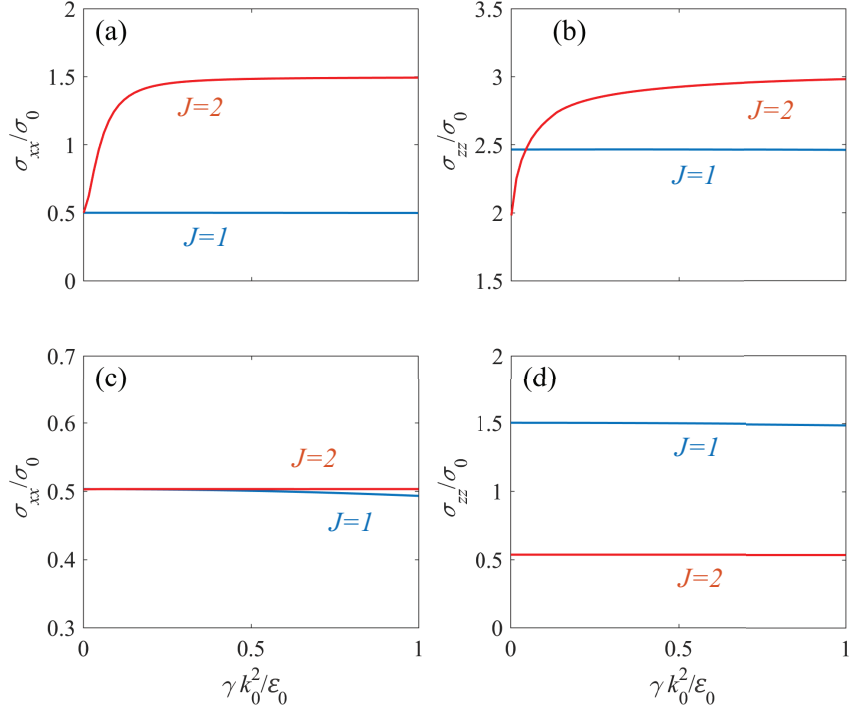


FIG. 6: Power-law exponent of σ_{xx} and σ_{zz} as a function of $\gamma k_0^2/\epsilon_0$ (a), (b) in the NI phase and (c), (d) at the transition between the NI and WSM phases for $J = 1$ (blue) and $J = 2$ (red). For $J = 2$ in the NI phase, the deviation of the power-law from that obtained within the $\gamma = 0$ approximation is significant because the quadratic in-plane energy dispersion is comparable to the quadratic γ term.

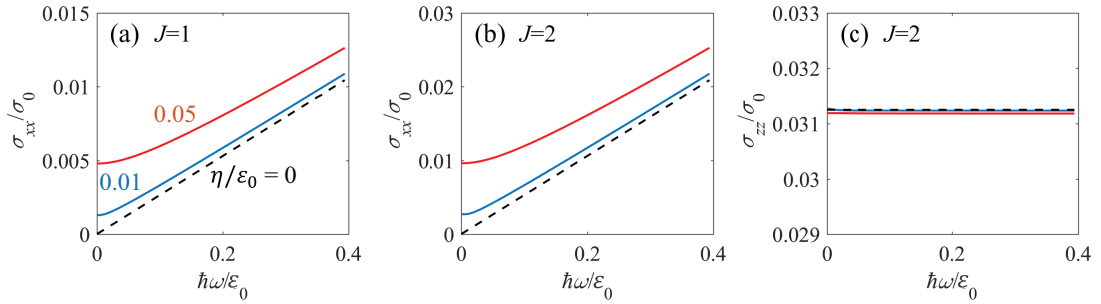


FIG. 7: Calculated longitudinal optical conductivities in the presence of disorder for (a) $J = 1$ and $J = 2$ in the (b) in-plane and (c) out-of-plane directions. Above the frequency scale set by the impurity potential, the characteristic frequency dependence presented in this work remains valid. Here, we set $\mu = 0$ and use several values of the broadening $\eta/\epsilon_0 = 0, 0.01, 0.05$ for calculation.

C. Chemical potential

Chemical potentials of m-WSMs do not need to stay at a Weyl node, and they vary depending on materials. Figure 8 shows calculated optical conductivities with zero and finite chemical potentials. As explained in the main text, a finite chemical potential μ away from a Weyl node produces a gap with a size of $2|\mu|$ due to Pauli blocking in interband transitions and a Drude peak near zero frequency from intraband transitions. Above the gap size, however, the optical conductivity follows the characteristic frequency dependence described in the main text.

D. Tilt

In general, a Weyl node can be tilted breaking particle-hole symmetry. First, let us consider possible forms of a tilt Hamiltonian allowed for multi-Weyl nodes. As mentioned in the main text, multi-Weyl nodes are protected by

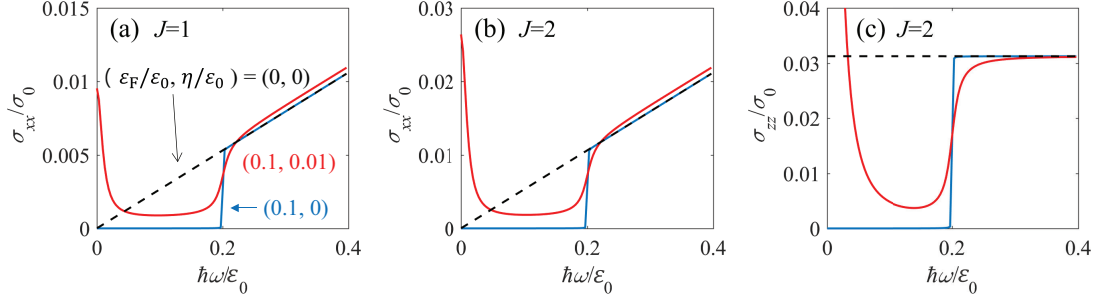


FIG. 8: Calculated longitudinal optical conductivities with chemical potentials $\mu = 0$ (dashed) and $\mu = 0.1\varepsilon_0$ (solid) for (a) $J = 1$ and $J = 2$ in the (b) in-plane and (c) out-of-plane directions. For finite μ , in addition to results with $\eta = 0$ (blue), we present results with non-zero $\eta = 0.01\varepsilon_0$ (red) to induce a Drude peak with a finite width due to impurities. Above the frequency set by the gap with a size of $2|\mu|$, the optical conductivity follows the characteristic frequency dependence described in the main text.

point group symmetry. Assume that a multi-Weyl node is protected by an n -fold rotation along the k_z axis, where $n = 2, 3, 4, 6$ is restricted by lattice. Then a tilt Hamiltonian near a node point $\mathbf{k} = 0$ is given by $H_t = h(\mathbf{k})\sigma_0$. Following Fang *et al.* [1], we consider the functional form of $h(\mathbf{k})$ constrained by the n -fold rotational symmetry. Note that H_t is proportional to an identity matrix σ_0 , thus $h(\mathbf{k})$ does not change its form by rotation, leading to the constraint $h(R_n\mathbf{k}) = h(\mathbf{k})$, where R_n is the 3D rotation matrix for the n -fold rotation. Expressing \mathbf{k} as $\mathbf{k} = (k_+, k_-, k_z)$ where $k_{\pm} = k_x \pm ik_y$, $R_n\mathbf{k}$ is given by

$$R_n\mathbf{k} = (k_+e^{i2\pi/n}, k_-e^{-i2\pi/n}, k_z). \quad (44)$$

Thus, from the constraint by the n -fold rotational symmetry, we have

$$h(k_+, k_-, k_z) = h(k_+e^{i2\pi/n}, k_-e^{-i2\pi/n}, k_z). \quad (45)$$

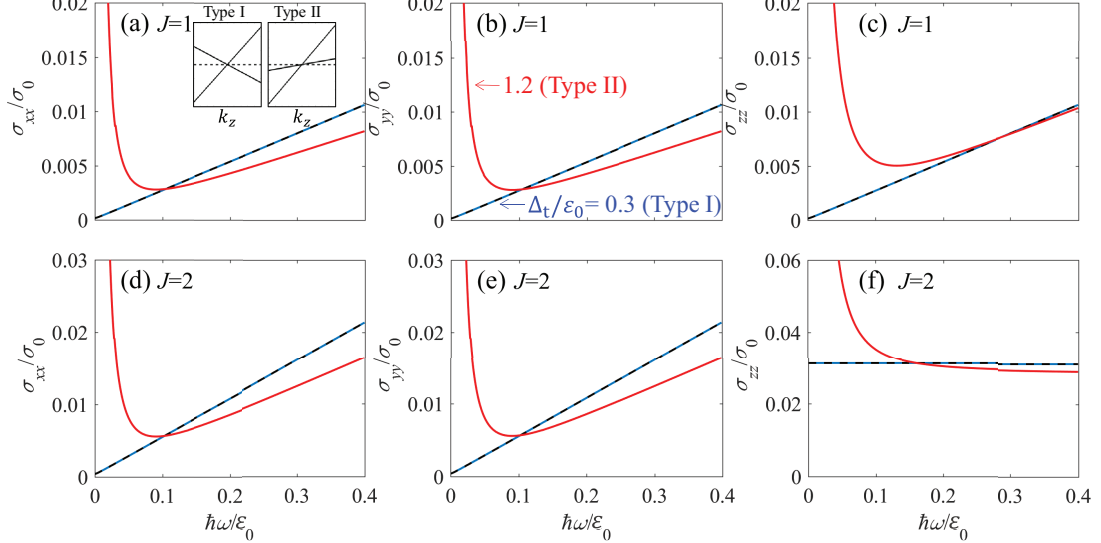


FIG. 9: Calculated longitudinal optical conductivities for (a)-(c) $J = 1$ and (d)-(f) $J = 2$ for several values of tilt $\Delta_t/\varepsilon_0 = 0$ (black dashed), 0.3 (blue solid), 1.2 (red solid), where $\Delta_t = \hbar v_t k_0$. An inset to (a) shows the energy dispersion along the tilt direction. Here, $\eta = 0.001\varepsilon_0$ is used for the calculation.

To obtain an approximate effective Hamiltonian of the tilt term, assume an expansion of

$$h(k_+, k_-, k_z) = \sum_{n_1, n_2} C_{n_1 n_2} k_+^{n_1} k_-^{n_2} + \hbar v_t k_z, \quad (46)$$

where $C_{n_1 n_2}$ is an expansion coefficient and v_t is the tilt velocity along the k_z direction. Then from Eq. (45), we find $e^{i2\pi(n_1 - n_2)/n} = 1$ or $n_1 - n_2 = 0 \pmod{n}$ for non-vanishing $C_{n_1 n_2}$. Thus the lowest order expansion of k_+ and k_- is

given by $n_1 = n_2 = 1$ irrespective of n . Then the tilt Hamiltonian to the lowest order has a form of

$$h(\mathbf{k}) \approx C_{11}(k_x^2 + k_y^2) + \hbar v_t k_z. \quad (47)$$

Here we used $k_+ k_- = k_x^2 + k_y^2$. This means that the in-plane tilt of multi-Weyl nodes cannot be linear, and the leading order tilt is a linear term along the direction of the rotational symmetry axis.

To understand the effect of tilt on the optical conductivity of m-WSMs, consider a tilt term given by $H_t = \hbar v_t k_z \sigma_0$. Figure 9 shows the optical conductivity of tilted multi-Weyl nodes. For both $J = 1$ and $J = 2$, tilt hardly affects the optical conductivity unless tilt is large enough that the system becomes type II [2] ($v_t > v_{\parallel}$). When the system becomes type II Weyl semimetals, the Drude peak becomes significantly enhanced due to the formation of an electron-hole pocket whose size is comparable to the lattice scale ($\sim 1/a$). At sufficiently high frequencies, however, the optical conductivity recovers its original characteristic frequency behavior, as shown in Fig. 9.

-
- [1] C. Fang, M. J. Gilbert, X. Dai, and B. A. Bernevig, Multi-Weyl Topological Semimetals Stabilized by Point Group Symmetry, *Phys. Rev. Lett.* **108**, 266802 (2012).
 [2] A. A. Soluyanov, D. Gresch, Z. Wang, Q. S. Wu, M. Troyer, X. Dai, and B. A. Bernevig, Type II Weyl semimetals, *Nature (London)* **527**, 495 (2015).